Multiscale Femoral Neck Imaging and Multimodal Trabeculae Quality Characterization in an Osteoporotic Bone Sample

Enrico Soldati, Flavy Roseren, Daphne Guenoun, Lucia Mancini, Emilio Catelli, Silvia Prati, Giorgia Sciutto, Jerome Vicente, Stefano Iotti, David Bendahan, et al.

materials

MDPI

Article

Multiscale Femoral Neck Imaging and Multimodal Trabeculae Quality Characterization in an Osteoporotic Bone Sample

Enrico Soldati [1,2,3,*], Flavy Roseren [3], Daphne Guenoun [3,4], Lucia Mancini [5,6], Emilio Catelli [7], Silvia Prati [7], Giorgia Sciutto [7], Jerome Vicente [1], Stefano Iotti [8,9], David Bendahan [2], Emil Malucelli [8] and Martine Pithioux [3,10]

1 Aix Marseille University, CNRS, IUSTI, 13453 Marseille, France
2 Aix Marseille University, CNRS, CRMBM, 13385 Marseille, France
3 Aix Marseille University, CNRS, ISM, 13288 Marseille, France
4 Aix Marseille University, APHM, CNRS, ISM, Sainte Marguerite Hospital, Institute for Locomotion, Department of Radiology, 13274 Marseille, France
5 Elettra-Sincrotrone Trieste S.C.p.A, SS 14–km 1535 in Area Science Park, Basovizza, 34149 Trieste, Italy
6 Slovenian National Building and Civil Engineering Institute, Dimičeva ulica 12, 1000 Ljubljana, Slovenia
7 University of Bologna, Department of Chemistry "G. Ciamician", Ravenna Campus, Via Guaccimanni, 42, 48121 Ravenna, Italy
8 Università di Bologna, Department of Pharmacy and Biotechnology (FaBit), Via Zamboni 33, 40126 Bologna, Italy
9 National Institute of Biostructures and Biosystems, Viale delle Medaglie d'Oro 305, 00136 Roma, Italy
10 Aix Marseille University, APHM, CNRS, ISM, Sainte-Marguerite Hospital, Institute for Locomotion, Department of Orthopaedics and Traumatology, 13274 Marseille, France
* Correspondence: enrico.soldati@univ-amu.fr

check for updates

Citation: Soldati, E.; Roseren, F.; Guenoun, D.; Mancini, L.; Catelli, E.; Prati, S.; Sciutto, G.; Vicente, J.; Iotti, S.; Bendahan, D.; et al. Multiscale Femoral Neck Imaging and Multimodal Trabeculae Quality Characterization in an Osteoporotic Bone Sample. *Materials* **2022**, *15*, 8048. https://doi.org/10.3390/ma15228048

Academic Editor: Thierry Hoc

Received: 30 September 2022
Accepted: 9 November 2022
Published: 14 November 2022

Publisher's Note: MDPI stays neutral with regard to jurisdictional claims in published maps and institutional affiliations.

Abstract: Although multiple structural, mechanical, and molecular factors are definitely involved in osteoporosis, the assessment of subregional bone mineral density remains the most commonly used diagnostic index. In this study, we characterized bone quality in the femoral neck of one osteoporotic patients as compared to an age-matched control subject, and so used a multiscale and multimodal approach including X-ray computed microtomography at different spatial resolutions (pixel size: 51.0, 4.95 and 0.9 µm), microindentation and Fourier transform infrared spectroscopy. Our results showed abnormalities in the osteocytes lacunae volume (358.08 ± 165.00 for the osteoporotic sample vs. 287.10 ± 160.00 for the control), whereas a statistical difference was found neither for shape nor for density. The osteoporotic femoral head and great trochanter reported reduced elastic modulus (Es) and hardness (H) compared to the control reference (−48% ($p < 0.0001$) and −34% ($p < 0.0001$), respectively for Es and H in the femoral head and −29% ($p < 0.01$) and −22% ($p < 0.05$), respectively for Es and H in the great trochanter), whereas the corresponding values in the femoral neck were in the same range. The spectral analysis could distinguish neither subregional differences in the osteoporotic sample nor between the osteoporotic and healthy samples. Although, infrared spectroscopic measurements were comparable among subregions, and so regardless of the bone osteoporotic status, the trabecular mechanical properties were comparable only in the femoral neck. These results illustrate that bone remodeling in osteoporosis is a non-uniform process with different rates in different bone anatomical regions, hence showing the interest of a clear analysis of the bone microarchitecture in the case of patients' osteoporotic evaluation.

Keywords: Fourier transform infrared spectroscopy (FTIR); microindentation; magnetic resonance imaging (MRI); osteocytes lacunae; osteoporosis; X-ray computed microtomography (µCT)

1. Introduction

Bone is a dynamic tissue in which aged bone is being continuously resorbed and replaced by younger bone, so that mineral homeostasis and integrity of bone structure can be maintained [1]. This process, referred to as bone remodeling, is a multiscale process and

recent works have highlighted the major role of osteocytes in maintaining bone mass and volume. Osteocytes, the most abundant bone cells, are stocked in lacunar voids distributed throughout the entire bone are interconnected by canaliculi and play a role in the anabolic response to mechanical stimuli [1,2]. This osteocytes-mediated mechanism, called mechanotransduction, leads to the release of soluble factors involved in bone resorption or bone formation [3,4]. Considering that osteocytes are considered to be key regulators of skeletal homeostasis, their role in bone diseases has been suggested through changes in morphology and network [5]. In that context, several imaging modalities have been developed for osteocytes. Conventional microscopic 2D imaging techniques are limited by the lack of the third dimension [6–9]. Multiple 3D imaging modalities have been used [10–12] and among them, synchrotron radiation computed tomography (SR CT) at the micro- and nanoscale levels is of interest, given that it can provide volumetric information and investigate the 3D material properties with a non-destructive approach [13–16]. Given the increasing interest in osteocytes, a large variety of imaging techniques providing different spatial resolutions have been used. However, data in human bone remain scarce and are generally limited to a very small field of view. On that basis, a complete morphological analysis of osteocytes lacunae (OL) would be of great interest, since changes could affect the bone remodeling process. Changes in lacunar shapes have been observed in pathologies such as osteopenia, osteopetrosis and osteoarthritis [17].

In particular, osteoporosis, one of the most common pathologies, is a systemic disease characterized by a reduced bone mineral density (BMD) and a thinning of both cortical and trabecular phase due to bone resorption, which usually leads to fragility fractures [17,18]. The increased susceptibility to fragility fractures usually accounts for the reduced bone strength and quality. While both determinants are tightly linked to several parameters related to bone geometry, architecture, mineralization, and remodeling, osteoporosis is still currently diagnosed on the basis of BMD measurements using dual-energy X-ray absorptiometry (DXA) [19]. BMD is considered to be an index of bone mass loss, and on that basis, as a predictor of the sensitivity to osteoporotic fractures. However, it has been acknowledged that bone strength depends not only on bone quantity, but also on its shape and hierarchical structure [19–21]. However, very few studies have assessed osteocytes morphology in osteoporosis [16].

Previous studies have shown that the bone post-yield behavior, characterizing the capacity to absorb the energy before failure, is linked to the organic phase and its alteration has been associated with changes in the mechanical behavior, making bones more ductile or brittle [22]. Moreover, the bone extracellular matrix (ECM), which plays an important role in the tissue rigidity, is highly related to the mechanical properties of the bone tissue [23]. In altered ECM, the mineral part of the bone will also be affected, leading to modulations in the mechanical behavior [22].

Recent studies have shown that the ECM is responsible for the mineralization process and influences the density of the crystal composition [24]. Hence, the bone multimodal analysis is of great interest since it would allow for characterization of the bone mechanical properties, level of mineralization, carbonate accumulation and collagen cross-links, providing reliable indicators of the bone material properties. The bone quality and mineralization have been also assessed using reference point indentation (RPI) [25], which is a microindentation technique able to directly measure mechanical properties in diseased bone samples [26–29]. However, further validation of this technique is required to assess the relation between RPI and bone material properties.

Although previous studies have assessed bone microarchitecture [21,30,31], composition [32–35], mechanical properties [36–38] and OL morphology and network [13,39,40], these characteristics have been usually investigated alone and in more accessible bone segments (cortical phase [37,41] tibiae [17,38], distal femur [31,32], vertebrae [34,36]). Therefore, an analysis combining all the previously presented characteristics on the trabeculae of same samples is of great interest to obtain a more comprehensive overview of the bone health state.

The present study aimed to characterize bone quality in the femoral neck region using a multiscale and multimodal approach including imaging by X-ray computed microtomography at different spatial resolutions, i.e., with a pixel size of 51.0, 4.95 and 0.9 µm, micro-indentation and Fourier transform infrared spectroscopy. The bone characterization of the osteocytes network, trabecular composition and mechanical properties could provide a better understanding of the bone quality, with direct implications in pre-clinical research, therapeutic strategy, and eventually clinical practice. We chose to assess the femoral neck region, given that femoral neck fractures amount to 14% of the overall occurring fragility fractures [18].

2. Materials and Methods

Femoral neck morphology was assessed using laboratory-based X-ray microtomography (µCT) and synchrotron radiation microtomography (SRµCT), providing an isotropic voxel size resolution of 51 and 4.95 µm, respectively. We also performed SRµCT scans of the femoral neck at a pixel size of 0.9 × 0.9 µm^2 in order to obtain a 3D quantification of OL. The combination of µCT and SRµCT allowed the bone analysis at different scales, therefore focusing on volume of interests (VOI), in particular VOI equal to 66,325 mm^3, 1042 mm^3 and 6.27 mm^3, respectively for isotropic voxel size resolutions of 51.0 µm, 4.95 and 0.9 µm. Low-resolution images were used for double purpose. First, image stacks have been visually inspected so as to identify all the target regions to be acquired at higher resolutions. These images were also analyzed so as to obtain all the derivable morphological information (see Appendix A). On that basis and considering that proximal femur fractures usually occur in the femoral neck, the analysis at 51.0 and 4.95 µm resolution was performed in the femoral neck. Then, the subsequent acquisitions at 0.9 µm resolution were performed in regions with the higher bone density according to the 4.95 µm resolution images. Finally, bone trabecular quality has been assessed using the microindentation and the Fourier transform infrared spectroscopy. The workflow of the current experimental study is presented in Figure 1. These methods provided information related to trabeculae mechanical properties, mineralization and carbonate accumulation in several anatomical regions of the osteoporotic proximal femur. The corresponding results were compared to those obtained in a healthy bone sample.

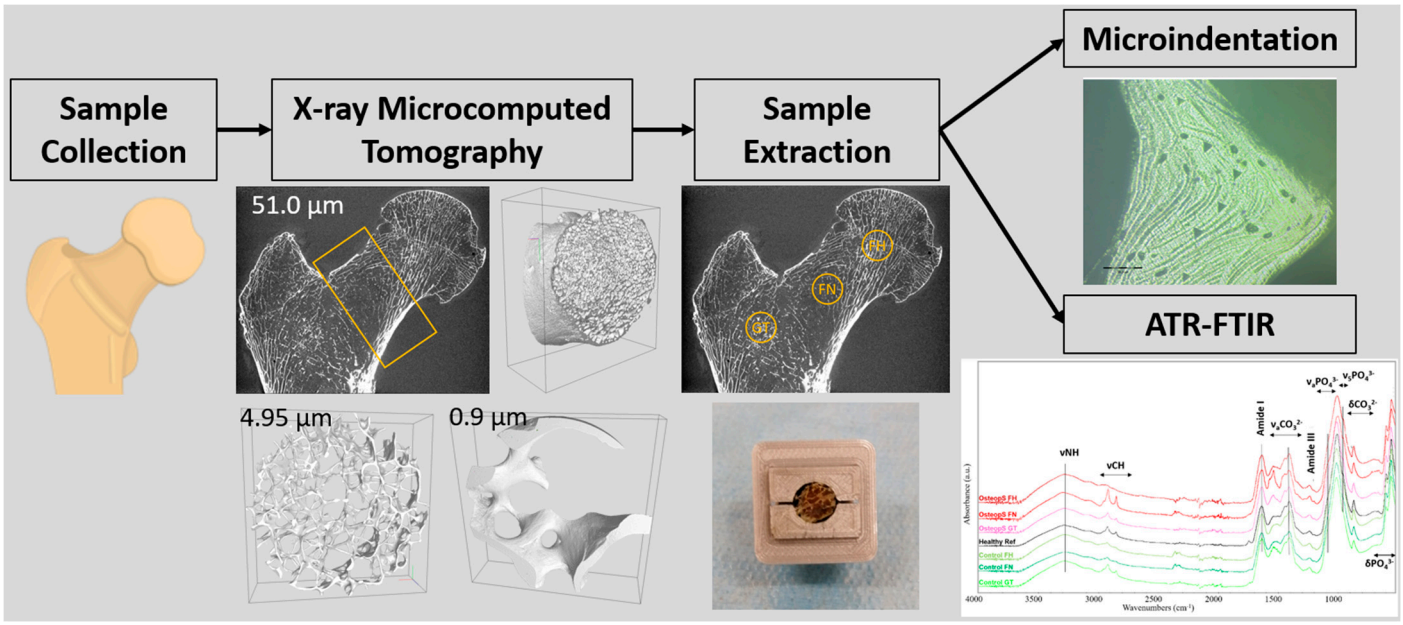

Figure 1. Experimental study workflow.

2.1. Sample Collection and Preparation

Bone collection was performed with the agreement of the local ethics committee and according to the 1975 Helsinki Declaration (revised in 2000). Both donors were female and, according to the DXA measurements, one bone sample was classified as osteoporotic, whereas the other one was classified as normal (Table 1). Samples were cut using a bandsaw along the axial direction right below the lesser trochanter (approximately 10 to 12 cm section proximal to the femur head), and the specimen were then stored at −25 °C.

Table 1. Sample description.

	Gender	Age (y)	Leg Pos	Height (m)	DXA (g/cm^2)		
					Total	Neck	Troch. [2]
Control	Female	95	Right	1.63	0.939	0.898	0.883
OsteopS [1]	Female	96	Right	1.65	0.480	0.423	0.419

[1] OsteopS stands for Osteoporotic sample. [2] Troch. Stands for Great Trochanter.

2.2. Sample Extraction and Preparation for Microindentation Test

Using a drill press, equipped with a hollow tip (10 mm internal diameter) and under constant water irrigation, three small samples were extracted from each proximal femur so as to characterize the mechanical properties of the lamellar bone. These regions were chosen in the great trochanter (GT), the femoral neck (FN) and the femoral head (FH). The samples were harvested perpendicular to the coronal plane and kept frozen at −25 °C. The micro-indentation protocol was performed as previously described [42]. Briefly, the surface of each specimen was consecutively polished (ESC-200-GTL, ESCIL® Chassieu, France) with carbide papers (P600, P1200, P2500) and multiple diamond slurries (6, 3, 1 and 0.25 µm). Prior to the mechanical assays, the sample preparation quality was validated using optical microscope Figure 2. Specimens were then stored in a solution containing calcium (50 mg/L) and sodium azide (0.01%) in order to prevent bone mineral matrix dissolution and collagen degradation [43]. They were kept refrigerated before indentation.

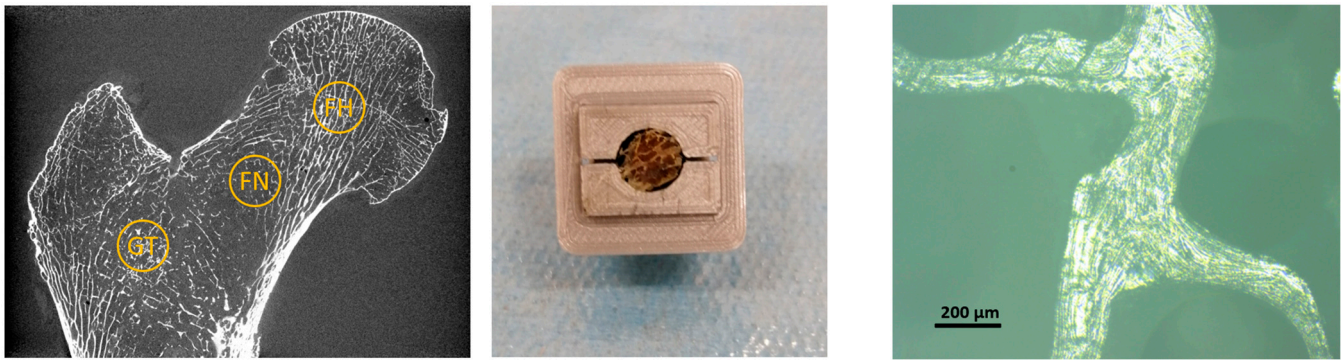

(**a**) (**b**) (**c**)

Figure 2. Sample extraction and preparation. (**a**) Localization of the three different bone regions extracted from each proximal femur, "GT" refers to great trochanter, "FN" refers to femoral neck and "FH" refers to femoral head; (**b**) trabecular sample stored in the designed sample holder after the sample preparation protocol; (**c**) optical microscopic investigation used to assess the efficacy of the preparation protocol before the microindentation assays.

2.3. X-ray Microtomography Measurements

The µCT scans of both proximal femurs were acquired using a Rx-Solution EasyTom XL ULTRA instrument [44] as previously described [45].

Propagation-based phase contrast SRµCT data were used to obtain the 3D virtual reconstruction of the bone microstructure at the microscale. The central core across the

whole length of femoral neck was imaged at the SYRMEP (SYnchrotron Radiation for MEdical Physics) beamline of the Elettra synchrotron facility (Basovizza [Trieste], Italy) using a filtered (1.5 mm Si +1 mm Al) polychromatic X-ray beam, delivered by a bending magnet source in transmission geometry and with a mean energy of 27 KeV. The detector used was a water-cooled, 16-bit, sCMOS macroscope camera (Hamamatsu C11440–22C) with a 2048 × 2048 pixels chip coupled with different GGG:Eu scintillator screens of different thickness, depending on the selected pixel size, through high numerical aperture optics. The effective pixel size of the detector was set at 4.95 × 4.95 μm^2 and 0.9 × 0.9 μm^2 using, respectively, a 45 and 17 μm thick scintillator screen, yielding a maximum field of view of about 10.1 × 10.1 mm^2 and 1.8 × 1.8 mm^2, respectively. The sample-to-detector (propagation) distance was set at 150 mm. A set of 1200 projections were recorded, with a continuous sample rotation over a 180-degree scan angle and an exposure time per projection of 2.5 s.

Each set of acquired raw images (projections) was processed using the SYRMEP Tomo Project (STP) software suite, developed in-house at Elettra [46] and based on the ASTRA Toolbox [47]. The tomographic reconstruction was performed using the filtered backpropagation algorithm, coupled to a filter [48] to reduce the so-called ring artefacts in the reconstructed slices. A single-distance phase retrieval algorithm was applied to projection images prior to reconstruction [49], setting the δ β parameter (ratio between the real and imaginary parts of the complex refraction index of the material under investigation) to 50 and 20 for images reconstructed with an isotropic voxel size of 4.95 and 0.9 μm^3, respectively.

2.3.1. Image Post-Processing and Analysis

The image post-processing and analysis have been performed using the software iMorph (iMorph_v2.0.0, AixMarseille University, Marseille, France) [50,51]. iMorph provides a 3D transformation map from which the aperture map can be derived. The aperture map provides, for each pixel of the bone/OL, the diameter of the maximal disk totally enclosed in the bone/OL and containing this voxel.

2.3.2. SRμCT (Voxel Size: 0.9 μm)

Thanks to the extremely small voxel size (0.9 μm), the image field of view was focused on a single trabecula (Figure 3d) and the OL became assessable. First, a 3D median filter, using a window size of 3 × 3 × 3 voxels, has been applied to denoise the image volumes. In order to binarize the image stack, the threshold that better differentiated the bone from the pores (OL and vascular canals) was selected manually from the gray levels' distribution of each volumetric image stack. Finally, a morphometric threshold of 27 voxels has been chosen to define the minimum number of voxels identifying an object, and these misclassified voxels were re-added to the solid phase. The bone porosity was measured as the percentage of the volume of the soft phase (small pores, OL and vascular canals) over the sum of the soft and bone phases. Second, the OL were identified as those regions composed by a volume in the 73 to 1000 μm^3 range, chosen in accordance with the mean and standard deviation of OL previously found in the literature [4,14]. In addition, this strategy allowed us to distinguish the OL from the vascular canals network, which was characterized by higher volumes (Figure 3e,f) [14,15]. The image processing effect (median filtering, manual thresholding, and morphometric analysis) for the OL characterization has been investigated and is discussed in the Appendix B. Finally, each OL was individually characterized using the volume, surface, size, shape, sphericity, and fractal anisotropy and as an interconnected network by evaluating its region of action. In particular, in each OL the principal axes (a, b and c) of the maximum inscribed ellipsoid have been calculated. On that basis, the OL shape was computed from the derivation of the aspect

ratios ($\frac{a}{b}$, $\frac{b}{c}$, $\frac{a}{c}$ and $\frac{a}{(b+c)}$). Then, the outer surface (S_{OL}) and the sphericity index (Fsph) [52] were derived, respectively, by the formula:

$$S_{OL} = 4 * \pi * (a^p b^p + a^p c^p + b^p c^p)^{\frac{1}{p}}, \; with \; p = ln(3)/ln(2)$$

$$Fsph = 6 * V_{OL} * \left(\pi / {S_{OL}}^3\right)^{0.5}$$

where V_{OL} is the OL volume. Moreover, the fractal anisotropy (FrAn) [53], which reflects the axonal diameter and is an extension of the concept of eccentricity of conic sections in 3 dimensions, normalized to the unit range, has been calculated using the formula:

$$FrAn = \sqrt{\frac{3}{2}} * \frac{\sqrt{(a-\lambda)^2+(b-\lambda)^2+(c-\lambda)^2}}{\sqrt{a^2+b^2+c^2}}, \; where \quad \lambda = (a+b+c)/3$$

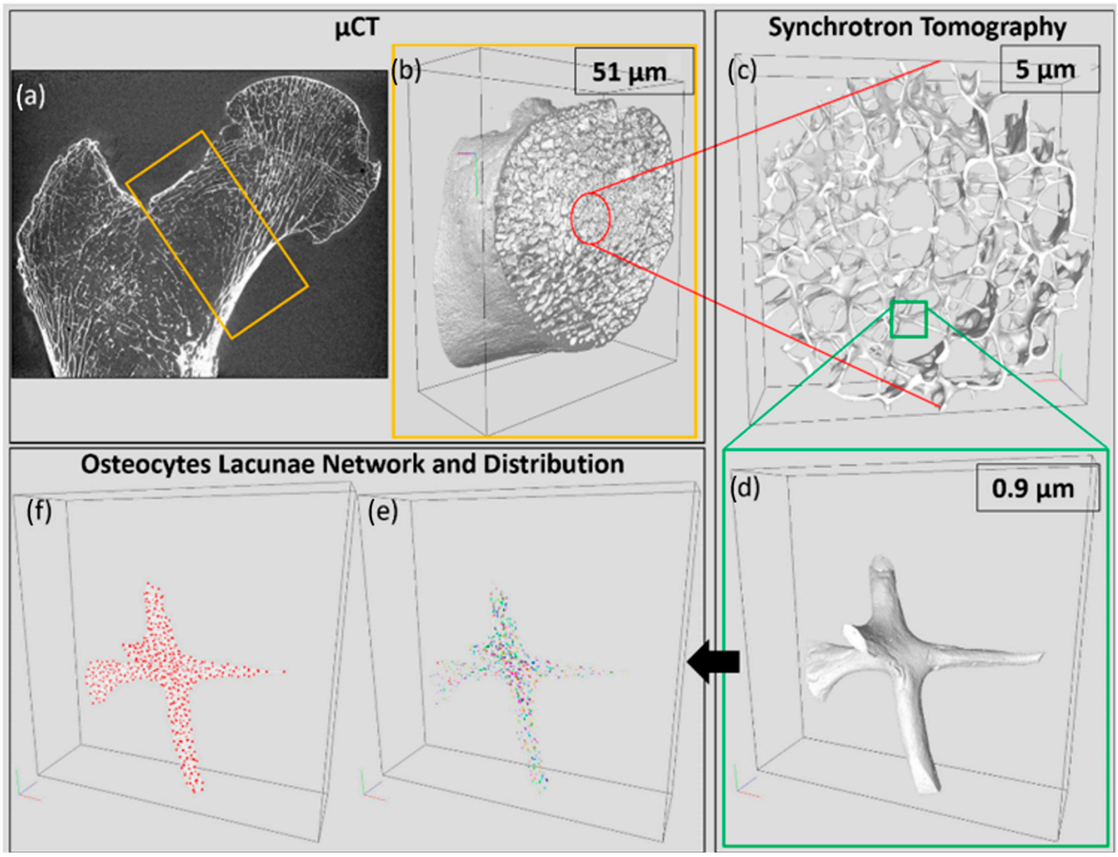

Figure 3. Multiscale characterization of femoral neck morphology acquired using µCT (voxel size: 51.0 µm) and SRµCT (voxel size: 4.95 and 0.9 µm). (**a**) Proximal femur coronal plane acquired using µCT at 51.0 µm showing the femoral neck ROI (orange rectangle) used to assess clinical-standard bone mineral density by dual-energy X-ray absorptiometry; (**b**) whole femoral neck acquired using µCT at 51.0 µm; (**c**) central core of the femoral neck trabecular phase scanned using SRµCT at 4.95 µm; (**d**) single trabecula acquired using SRµCT at 0.9 µm; (**e**) OL distribution and (**f**) OL network.

Finally, the region of action could be considered as a 3D bone, neighboring the OL, in which the osteocytes sense and transmit information. It was derived by applying the Voronoi map, which calculates the minimum path between the closest OL and differs from the OL density because it is calculated for each OL singularly.

2.4. Microindentation

The trabecular bone of the whole set of specimens has been characterized using a microindentation apparatus (Tester NHT^2, Anton Paar®, Switzerland and Austria) equipped with a sharp Berkovich diamond indenter (tip diameter: 120 nm, elastic modulus: 1141 GPa and Poisson's ratio: 0.07) in a thermally controlled room at 23 °C and on a pneumatic antivibration table. For the indentation tests, the sample was set in a watertight support filled with calcium buffered saline up to the level of the polished surface. A total of 40 points were selected using a ×20 microscopic objective on five different trabeculae located on the polished surface of the sample. Points were placed in the trabecular centerline to avoid any border effect and verified at magnitude x100 to avoid any surface irregularities (i.e., porosity). Before each set of indentation, a calibration session test was made on a fused silica reference sample. The mean corresponding values were 71.3 ± 1.6 GPa while the reference data was 72 GPa.

A trapezoidal loading profile (30 s: 60 s: 30 s, max load 40 mN) has been applied, as shown in Figure 4, in the polished surface of each sample. The 60 s plateau time was chosen from preliminary tests because wet tissues display a more viscous mechanical behavior. The sample hardness (H) and elastic modulus (Es) were calculated using the Oliver and Pharr method [54]. In this study, the Poisson's ratio was assumed to be 0.3, since the relative error, determined by varying the Poisson's ratio from 0.2 to 0.4, was found to be less than 8% in elastic modulus [23,55].

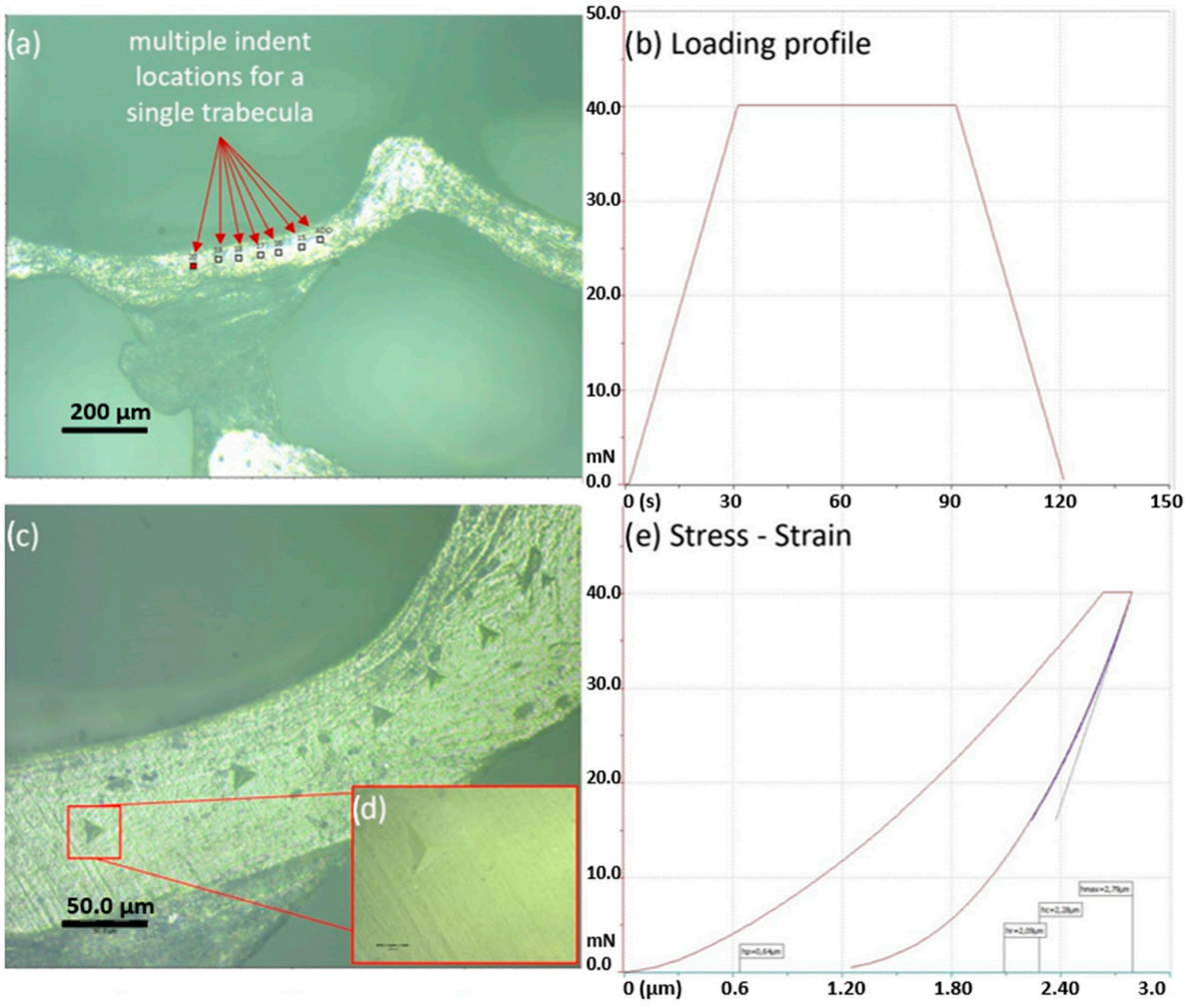

Figure 4. Trabeculae micro indentation. (**a**) Manually placed indent locations for each selected trabecula, (**b**) indentation trapezoidal loading profile, (**c**) stress–strain plot showing a single load–unload cycle, (**d**) indented area and (**e**) view of a single indent at original magnification ×100.

The mean and standard deviation for elastic moduli and the hardness, both expressed in GPa, were obtained for the osteoporotic subject and the control.

2.5. Fourier Transform Infrared Spectroscopy

The attenuated total reflection Fourier transform infrared (ATR-FT-IR) measurements were obtained using a Thermo Nicolet iS50 FTIR spectrometer (Thermo Fisher Scientific Co., Waltham, MA, USA) equipped with a deuterated triglycine sulphate (DTGS) detector. The ATR spectra were recorded using a diamond ATR Smart OrbitTM accessory (from Thermo Optec) in the Mid-IR spectral range 4000–525 cm^{-1}, averaging 64 scans for each measure and 64 scans for the background. The spectral resolution is 4 cm^{-1}. For each bone sample, a small fragment was collected and analyzed. The fragments were first ground in an agate mortar, and the powder obtained was successively placed on the ATR diamond crystal. Pressure was applied on the powder to optimize the contact with the diamond crystal. Several replicate spectra were acquired for each fragment. The spectra selected for interpretation were those which presented the highest signal-to-noise ratio.

A qualitative analysis of the spectra has been conducted considering the range 527–1800 and 2550–4000 cm^{-1}, where the most important features connected to bones component are visible. Generally speaking, the phosphate features of hydroxyapatite ($Ca_{10}(PO_4)_6(OH)_2$), the constituent of bones, show the main bands in the region 1050–1100 cm^{-1} (antisymmetric PO_4^{3-} stretching ν_a). Additional bands of the compound are at about 962 cm^{-1} (symmetric PO_4^{3-} stretching, ν_s) and between 660–520 cm^{-1} (in-plane PO_4^{3-} bending mode, δ_{ip}) [56–58]. Bones also have a carbonate group (CO_3^{2-}) allocated in the hydroxyapatite lattice. The infrared bands of carbonate are visible in the region 890–860 cm^{-1} (out-of-plane CO_3^{2-} bending mode, δ_{oop}) and 1400–1550 cm^{-1} (antisymmetric CO_3^{2-} stretching, ν_a) [57,59]. Apatite from natural bones may also contain a relevant amount of proteins. The presence of such an organic compound is visible from the CH and NH bands, respectively, at around 2800–3000 cm^{-1} and 3300 cm^{-1} (antisymmetric stretching, ν_a) and additionally, from the more specific bands connected to the proteinaceous-based vibrational modes at 1637 (Amide I), 1550 (Amide II), and 1239 cm^{-1} (Amide III) [60–62].

It is well known that the carbonate group (CO_3^{2-}) in bones' hydroxyapatite is present as a replacement of either PO_4^{3-} or OH- groups. When the substitutions happen at PO_4^{3-} sites, the compound is defined as B-type carbonated apatite (B-CAp); if the substitution is at OH- sites, the compound is an A-type carbonated apatite (A-CAp) [63,64]. According to several IR spectroscopic studies on synthetic apatite, the B-type is recognized by a doublet at ~1410 and ~1465 cm^{-1} (antisymmertric CO_3^{2-} stretching, ν_a) together with a signal at 870 cm^{-1} (out-of-plane CO_3^{2-} bending mode, δ_{oop}); conversely, the A-type is identified by a doublet at ~1456 and ~1540 cm^{-1} (antisymmertric CO_3^{2-} stretching, ν_a) and a signal at 880 cm^{-1} (out-of-plane CO_3^{2-} bending mode, δ_{oop}) [56,63–65]. The identification of A-type or B-type in biological apatite is more complex, as the IR characteristic signatures may be covered by the bands of other compounds. Ren at al. correctly pointed out that the peak at ~1546 cm^{-1}, the characteristic signature of A-type, can be masked by the Amide II of collagen [56]. Moreover, the bands at 1410, 1455 and 880 cm^{-1} should be used carefully for the identification of Cap, since similar bands were observed in other carbonate species adsorbed onto the apatite surface and not in the lattice [56].

Band assignation is also of a certain difficulty for the A or B type when A and B carbonate are present together in the apatite lattice. Considering the 1400–1550 cm^{-1} region, a synthetic sample of the AB-type showed a single band at 1460 cm^{-1} that accounted for the contribution of two overlapped signals: the low-frequency ν_a band of the A doublet and the high-frequency ν_a band of the B doublet; the other ν_a bands revealed a shift in the wavenumbers compared to the pure B and A standards [64]. Similar assignation was considered by Pedrosa et al. for the bands of male and female femoral bone hydroxyapatite: the band at 1450 cm^{-1} is assigned to the type A + B carbonate, while the B type is recognized by the 1415 cm^{-1} band [66]. In some spectra of biological apatite, the above-mentioned band at 1460 cm^{-1} is observed as two signals: a band at 1450 and a shoulder at 1465 cm^{-1} [56].

According to several researchers, the signal at 1465 cm^{-1} may be assigned to the B-type and the one at 1450 cm^{-1} to the A type [56,58,67]. This assignation, however, is not without controversy [68,69]. Regarding the carbonate bending region between 860–890 cm^{-1} (δ_{oop} CO_3^{2-}), the AB-type usually shows a doublet; several researchers agreed to assign the band at 880 cm^{-1} to the A-type and the one at 872 cm^{-1} to the B-type [58,64,70]. The predominance of B-type in AB-type is possible, and was observed in a study conducted on cadaveric femur of a 39 yrs male [69]. In the study, Figueiredo et al. assigned the bands 1410, 1445 cm^{-1} and 871 cm^{-1} to the B-type apatite, while the band at 880 cm^{-1}, shoulder, was assigned to type A [69].

2.6. Statistical Analysis

For the morphological parameters of each OL, student *t* tests were used to assess whether the osteoporotic samples differed significantly from the control samples. For each VOI, the potential relationships between the OL characteristics and the bone volume were assessed using the spearman coefficient of correlation (R^2).

Regarding the trabeculae mechanical parameters, given the non-normal distribution identified through a Shapiro–Wilk test, non-parametric tests were used to assess the effects of ROIs (femoral head vs. femoral neck vs. great trochanter). Kruskal–Wallis tests and multiple pairwise comparisons with a Bonferroni correction were performed using Dunn's tests. Mann–Whitney U tests were used to assess the differences between osteoporotic and control samples.

3. Results

3.1. Osteocytes Lacunae Characteristics

OL morphological parameters, computed from the OL embedded in the solid bone phase, are summarized in Table 2 and Figure 5. The number of OL per bone volume was slightly lower (−3%) in the osteoporotic subject as compared to the control, whereas the mean OL density showed the opposite effect, with the osteoporotic subject having a higher density (+3%) as compared to the control. The Voronoi map showed that the osteoporotic subject did not have a statistically significant lower region of action (−5%) than the control (56.7 × 103 μm^3 vs. 59.6 × 103 μm^3). Moreover, the mean OL volume of the osteoporotic subject (358.1 μm^3) was statistically larger (25%) than the corresponding control value (287.1 μm^3). The larger OL volume was also illustrated in the principal axes (a, b and c) of the maximum inscribed ellipsoid inside the OL, which resulted in non-statistically significant 8% larger axes in the osteoporotic OL as compared to the control. In addition, the osteoporotic OL surface was statistically larger compared to the controls (225.5 ± 13.7 μm^2 vs. 195.0 ± 10.1 μm^2).

However, no statistical difference was found in the axes of the inscribed ellipsoid in the OL, nor in the OL shape, (the aspect ratios where the osteoporotic OL showed 1% greater a/b, a/c and a/(b + c) and no difference was assessed for b/c).

Moreover, although the mean sphericity index and the mean fractal anisotropy showed no statistical difference between the osteoporotic and the control subject (0% and 1%, respectively), the control showed a much larger variability for both the sphericity index (0.798 ± 0.009 vs. 0.795 ± 0.024) and the fractal anisotropy (0.467 ± 0.015 vs. 0.462 ± 0.023).

The OL volume and surface statistically differed between the osteoporotic subject and the control. Similarly, the second and third principal axes of the inscribed ellipsoid in the OL were different between the osteoporotic subject and the control. However, no statistical difference was identified for region of action, density, porosity, aspect ratios, sphericity index and fractal anisotropy.

Table 2. Morphometric parameters of osteocytes lacunae (OL).

Total Values		OsteopS	Control	Diff
Nb of Analyzed Regions		5	5	-
Bone Volume (mm^3)		0.28	0.45	-
OL Number		4030	6649	-
OL Volume (mm^3)		0.0016	0.0023	-
OL Density (10^4 mm^{-3})		1.44	1.49	−3%
Bone Porosity (%)		0.59	0.52	+13%
Mean Values		**OsteopS (mean ± SD)**	**Control (mean ± SD)**	**Diff**
OL Volume (μm^3)		358.08 ± 165.00	287.10 ± 160.00	25% *
OL Surface (μm^2)		225.53 ± 13.75	195.00 ± 10.11	16% *
Lacunar Density (10^4 mm^{-3})		1.60± 0.33	1.56 ± 0.16	3%
OL Region of Action (10^4 μm^{-3})		5.7 ± 2.7	6.0 ± 4.0	−5%
OL Principal Axes (µm)	a (length)	12.13 ± 0.46	11.18 ± 0.57	8%
	b (width)	6.68 ± 0.32	6.19 ± 0.13	8% *
	c (depth)	4.40 ± 0.13	4.09 ± 0.12	8% *
OL Shape (Ad)	a/b	1.90 ± 0.11	1.89 ± 0.09	1%
	b/c	1.54 ± 0.06	1.53 ± 0.06	1%
	a/c	2.85 ± 0.07	2.82 ± 0.17	1%
	a/(b + c)	1.13 ± 0.05	1.12 ± 0.05	1%
OL Sphericity (Ad)		0.80 ± 0.01	0.79 ± 0.02	0%
OL Fractal Anisotropy (Ad)		0.47 ± 0.02	0.46 ±0.02	1%

Data are reported as mean ± standard deviation. "OsteopS" refers to osteoporotic subject, "Diff" stands for difference between the osteoporotic subject and the control, and "Ad" refers to a-dimensional. * indicates a p value < 0.05.

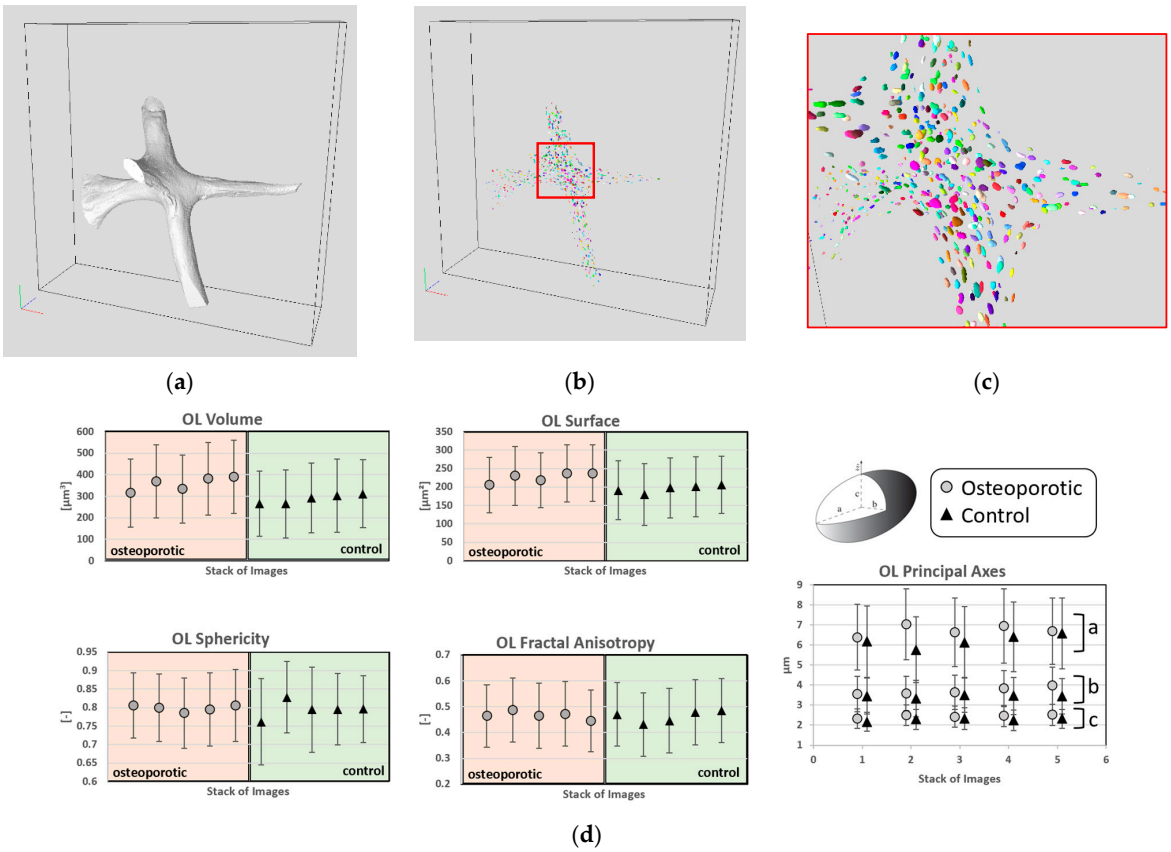

Figure 5. Osteocytes lacunae characteristics. "OL" refers to osteocytes lacunae. (**a**) morphology of a single trabecula, (**b**) visualization of the osteocytes lacunae embedded in the trabecula showed in (**a**), (**c**) magnification of the osteocytes lacunae in the center of (**b**,**d**) morphological analysis showing the volume, the surface, the sphericity, the fractal anisotropy and the principal axes computed from the osteocytes lacunae embedded in the solid bone of both the osteoporotic and the control sample.

In order to assess the potential relationship between the OL characteristics and the bone volume, Spearman correlation coefficients (R^2) were computed for each VOI. A very strong correlation was found between bone volume and the number of OL (R^2 = 0.97), while a good correlation was found for the region of action (R^2 = 0.59). A modest to poor correlation was found for OL volume (R^2 = 0.36), density (R^2 = 0.40), surface (R^2 = 0.27), sphericity (R^2 = 0.39) and fractal anisotropy (R^2 = 0.09).

3.2. Trabeculae Mechanical Properties

The microindentation assays allowed the characterization of the mechanical properties of the lamellar bone at the micro scale. The results presented in Figure 6 showed that the Es of the control FH had the highest mean value, which was significantly different from the other two regions, 62% higher compared to GT and 47% higher than FN (7.4 ± 2.5 GPa vs. 2.8 ± 1.3 GPa and 3.9 ± 1.2 GPa, $p < 0.0001$, respectively for the Es of FH, GT and FN). Interestingly, the GT showed the lowest Es mean value, which was significantly different ($p < 0.001$) than the Es in the FN area. In the OsteopS group, Es computed in the GT (2.0 ± 0.6 GPa) was significantly different as compared to the corresponding values in FH (3.9 ± 1.3 GPa) and FN (3.5 ± 1.4 GPa). In addition, Es values computed in FH and GT of the control were significantly higher as compared to the corresponding values in the osteoporotic subject (mean Es was 48% higher in FH ($p < 0.0001$) and 29% higher in GT ($p < 0.01$)). Surprisingly, in the FN, Es values were not affected by the osteoporotic status.

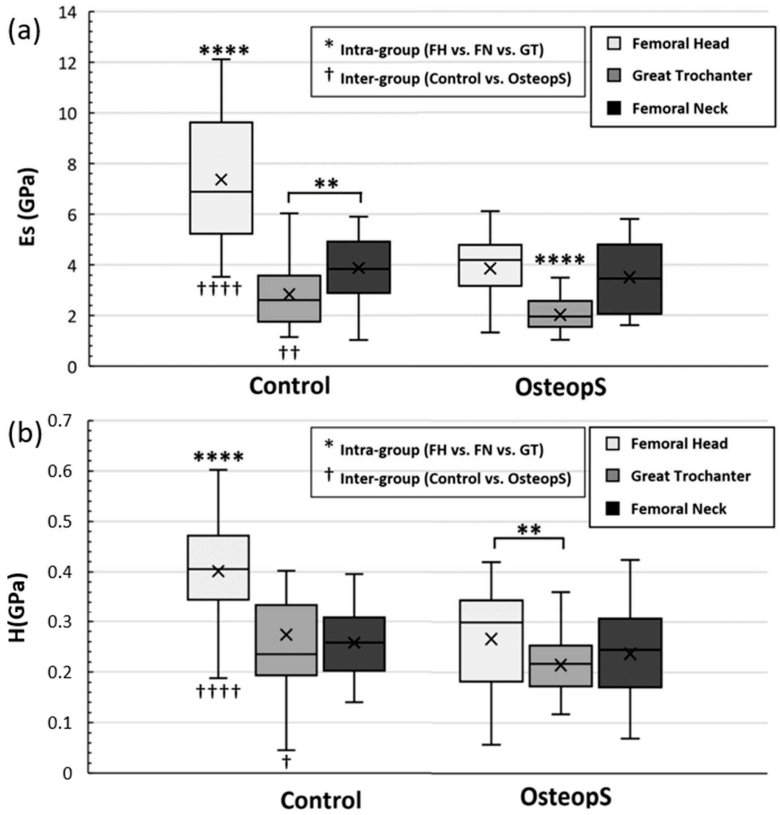

Figure 6. Whisker plot of (**a**) elastic modulus (Es) and (**b**) hardness (H) obtained using microindentation on trabecular bone specimens. (**a**) Representation of intra-group variation of elastic modulus. On the left the differences between the three ROIs in the control subject are presented, and on the right are the differences for the osteoporotic subject. (**b**) Representation of intra-group variation of hardness. On the left are presented the differences between the three ROIs in the control subject and on the right the differences for the osteoporotic subject. * represents the variability between different region of the same group (intra-group), ** $p < 0.01$ and **** $p < 0.0001$. † represents the variability between same regions of different group (inter-group) † $p < 0.05$, †† $p < 0.01$ and †††† $p < 0.0001$.

As illustrated in Figure 6b, in the control sample, hardness in FH was significantly larger ($p < 0.0001$) than the corresponding values in GT (+32%) and FN (+36%), whereas hardness values in GT and FN were similar. For the osteoporotic sample, hardness differed in FH (0.266 ± 0.099 GPa) and GT (0.215 ± 0.059 GPa). Moreover, similarly to Es intergroup differences, the H intergroup differences presented significant differences in the FH and GT, while no significant differences were obtained in the FN.

The H mean values obtained in the control FH and GT were, respectively, 34% ($p < 0.0001$) and 22% ($p < 0.05$) higher as compared to those from the osteoporotic sample.

3.3. ATR-FTIR Results

The ATR-FT-IR spectra of the bones fragment are reported in Figure 7a. One can identify that the main band of phosphates (1010 cm^{-1}) of the OsteopS FN and FH were slightly shifted as compared to the controls. The other signals connected to the phosphates (1087, 960, 599, 555 cm^{-1}) did not show significant changes. Similarly, the bands of Amide I (1637 cm^{-1}) and Amide III (1239 cm^{-1}) related to the proteinaceous component remain unchanged.

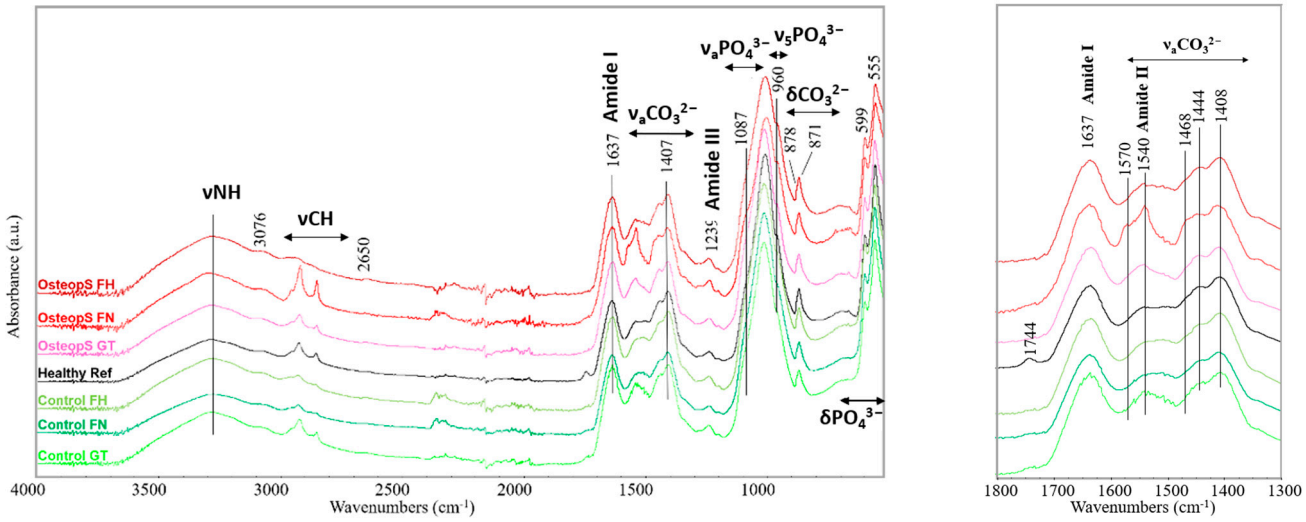

Figure 7. (**a**) ATR-FTIR spectra of the whole set of subjects and subregions. "OsteopS" refers to osteoporotic sample (S08); "Healthy Ref" refers to a refence sample of a healthy 61-year-old male; "FH" refers to femoral head, "FN" refers to femoral neck; "GT" refers to great trochanter. (**b**) Focus in the Amide I, Amide II and carbonate region (1300-1800 cm^{-1}).

Some slight differences can be noted in the region 1400–1550 cm^{-1}, where the anti-symmetric stretching of the carbonate apatite group falls (Figure 7b). The carbonate peak appears in both osteoporotic and control samples and the band at 1407 and 871 cm^{-1}, suggesting the presence of B-type carbonated apatite.

All the specimens presented a band at 1444 cm^{-1} followed by a shoulder at 1468 cm^{-1} that could be assigned to the A-type and B-type, respectively [56], although this is with some uncertainty.

The band at 1540 cm^{-1}, indicating the presence of A-type carbonated apatite, was not evaluable due to the band overlapping with the Amide II band. The band overlapping represents a well-known difficulty in peak attribution [56], which hampers the recognition of the presence of the A-type apatite. Only the shoulder at 878 cm^{-1} may suggest the presence of the A-type carbonate apatite in all the samples. In summary, the above-mentioned bands could point to the presence of AB-type apatite in all the analyzed samples.

Only in the FN sample of the osteoporotic subject, the amide II band appears different, showing a sharp signal at about 1540 cm^{-1} with additional peaks at 1576 and 1570 cm^{-1}.

The band's interpretation at 1540 cm^{-1} seems complicated in this case, as the contributions from the amide II band, the v3 of CAp type-A, and metal carboxylates may occur and overlap. In particular, the presence of metal carboxylates could be supported by the simultaneous signals at 1540, 1576, and 1570 cm^{-1}, together with the high intensity of the CH stretching at 2800–3000 cm^{-1}. Calcium carboxylates, whose absorption bands are reported in [71] and fall at 1538 and 1576 cm^{-1}, could be reasonably formed from the degradation of the fatty tissue of the human body [72].

4. Discussion

The multiscale and multimodal investigation of two femoral necks belonging to an osteoporotic subject and a healthy gender- and aged-matched subject undertaken in this study can be of great interest for a reliable assessment of the bone quality using a hierarchical approach to assess bone microarchitecture, trabecular mechanical properties, tissue composition, and OL characterization. The microindentation and the FTIR came to an additional support, respectively assessing the differences in the trabeculae mechanical properties and trabecular Hydroxyapatite composition between different proximal femur regions of the same sample and among different subjects (osteoporotic vs. gender and aged matched control).

This methodology allows the acquisition and the analysis of the femoral neck cortical and trabecular phase, the investigation of OL morphology and organization, the assessment of the local quantitative mechanical properties of the trabeculae and the qualitative characterization of the bone composition and mineralization. This experimental study would provide bone characteristics that cannot be included in clinical studies, although they are fundamental to obtaining a comprehensive overview of the bone quality with direct implications in computational studies [73], pre-clinical research, therapeutic strategy, and eventually clinical practice.

The high -ontrast and spatial resolution SRμCT made the OL visible and characterizable. In this study, OL differences have been assessed between the osteoporotic and the control in the OL volume, surface, and in the total solid phase porosity. However, no differences in the OL shape, sphericity and fractal anisotropy have been observed. Moreover, no statistical difference was assessed, considering the OL as an interconnected network, since OL region of action and density values between the two subjects were in the same range. Previous studies have investigated OL morphology in the cortical phase of femoral diaphysis [13–15], proximal tibiae [17] and iliac crest [6], however few studies have assessed the OL morphology in the trabecular bone phase. In a study conducted on the femoral diaphysis of 7 human cadavers (female, aging 75 ± 15 years old) scanned by synchrotron radiation nanotomography (nano-CT) at a voxel size of 120 nm, Peyrin et al. reported a mean OL volume and surface of 315.6 ± 51.7 μm^3 and 326.0 ± 50.0 μm^2, respectively [13]. Moreover, the principal axes of the inscribed ellipsoid were a = 16.7 ± 1.8, b = 79.0 ± 1.0 and c = 4.6 ± 0.7 μm. They also reported an OL density of 3.2 ± 1.2 × 104 mm^{-3} and average volume of each Voronoi cell or region of action of 2.6 ± 0.6 × 104 μm^{-3}. The differences in the region of action, which were almost double in our case, could be explained by the different bone region (cortical femoral diaphysis vs. trabecular femoral neck). Similar results were reported by Dong et al. on a study conducted on 13 cortical specimens from the femoral mid-diaphysis of two female donors scanned using SRμCT at a voxel size of 1.4 μm; the mean volume and surface were in the range of 409.5 ± 149.7 μm^3 and 336.2 ± 94.5 μm^2, respectively [14]. Moreover, they reported that the average dimensions were of 18.9 ± 4.9 μm in length, 9.2 ± 2.1 μm in width and 4.8 ± 1.1 μm in depth. In another study conducted on proximal tibial trabecular specimens extracted from 3 middle-aged women, respectively affected by osteoarthritis, osteopenia due to rheumatoid arthritis and osteopetrosis, and scanned using an industrial high-resolution nano-CT system at 580 nm^3, Van Hove et al. reported differences in OL shape between different pathologies, with the osteopenic subject presenting relatively large and round OL [17]. Moreover, they suggested that the differences in 3D morphology of osteocytes and their lacunae in long bones of

different pathologies with different BMD might reflect an adaptation to matrix strain due to different external loading conditions. In our case, although the osteoporotic and the control had different BMD, no difference in the OL shape was assessed, which might be due to the fact that both subjects were more than 90 years old and therefore one could suggest a reduced mobility in both cases. To further support this hypothesis, Van Oers et al. reported that osteocytes resulted in alignment to collagen fibres which are affected by the loading mode, moreover suggesting that variation in the lacunar and osteocytes shape undoubtedly affects the osteocytic mechanosensation and subsequent control of bone remodeling [4].

Mechanical loading is an essential stimulus for skeletal tissues. Osteocytes are primarily responsible for sensing mechanical stimuli in bone and for orchestrating subsequent responses. This is critical for maintaining homeostasis, and responding to injury/disease [2]. The microindentation results showed statistical differences in the trabeculae Es and H, depending on both their proximal femur anatomical location and bone health state. The FH showed greater Es and H compared to the other two bone regions investigated, moreover, they also showed a statistical difference between them in terms of bone health state. Although reporting the lowest Es and H, the GT showed similar results to FH. This was not the case for the FN, in which no differences were assessed between healthy and osteoporotic samples.

To the best of our knowledge, trabecular data on osteoporotic bone at the femoral neck could not be found in the literature, and only few studies have been found investigating the trabeculae mechanical properties in this regions [74–76]. Hoffler et al. conducted a study on 10 FN trabeculae (male between 40 and 85 years old), in which mean Es of at 8.57 ± 1.2 GPa and H of 0.37 ± 0.05 GPa were assessed. However, differences could be explained by the harvesting of the anatomical site which were closer to the cortical bone than in our case [76]. Moreover, KoKot et al. and Pawlikowski et al., on a study conducted, respectively, on 8 healthy FH (fame and female, 60+ years old) and 25 FH (male and female, 67 ± 9 years old) affected by osteoarthritis, and both using comparable microindentation protocols (trapezoidal loading profile, maximum loading = 500 mN, loading rate = 500 mN/min, holding time = 20 s), reported similar Es and H [77,78]. In particular, the Es and H reported were, respectively, 8.1 ± 1.4 GPa and between 0.30 and 0.50 GPa [77] vs. 7.4 ± 2.5 GPa and 0.40 ± 0.12 GPa in our case for the healthy subject, and 4.8 ± 1.1 GPa and 0.11 ± 0.02 GPa [78] vs. 3.9 ± 1.3 GPa and 0.27 ± 0.05 GPa in our case for bones characterized by an altered remodeling process (osteoarthritis vs. osteoporosis). The slightly lower values obtained in our study could be explained by differences in the preparation protocol (embedded in exothermic resin [74,76] vs. stored in a optimized support in our case) and/or indentation protocol (different maximum loading [75,77,78], holding time of the maximum load [77,78]). Supporting this hypothesis in the review article by Wu et al. has been reported a wide range of bone Es (1.3 GPa and 22.3 GPa) [23], moreover stating that this effect was due to the different scale of analysis (micro, sub-micro and nano scale), different sample preparation (dry vs. wet) [75], anatomical site and localization [79], and orientation of the indentation [80]. The patient age could also be a relevant factor, which could have led to an already altered ECM in both the healthy and the osteoporotic sample via an excessive bone remodeling process due to subjects' reduced mobility and leading, therefore, to a reduced bone stress profile. The study, conducted by Milovanovic et al. on 8 healthy FN specimens from female donors (5 young donors 32 ± 5 yrs, and 3 elderly donors 88 ± 6 yrs) using nanoindentation, supported this hypothesis and reported that elderly trabeculae expressed less elastic behavior (1.28 ± 0.16 GPa in the young vs. 1.97 ± 0.52 GPa in the elderly) at the material level. This makes elderly populations more vulnerable to unusual impact loads originating from a fall [81]. Therefore, we decided to repeat this microindentation assay on a sample harvested on a younger FN (61 years old), and the mean values obtained for Es were 7.6 ± 0.6 GPa and the H was 0.36 ± 0.05 GPa, which was in the same range found in previous studies [75–77]. For these reasons, knowing that mechanical parameters are correlated to ECM, composed by collagen, mineral, and non-collagenous proteins and since no differences have been derived

in the FN mechanical properties, one could suggest that the healthy and osteoporotic FN tissues were in the same bone remodeling state. Therefore, one could suggest that healthy FN was already impacted by an intensive bone remodeling process, because FN is one of the first regions impacted by osteoporosis. Overall, the results showed that bone remodeling is a non-uniform process that evolves at different rate depending on the bone anatomical region. An extensive investigation of the OL characteristics in both FH and GT regions could validate this hypothesis and reinforce the link between osteocyte network and bone quality.

The qualitative ATR-FTIR analysis aimed to assess the composition of osteoporotic and control samples, evaluating and reporting their significant differences. In this study, the bands at 1408 and 871 cm^{-1} suggest the presence of B-type apatite, and the band at 878 cm^{-1} suggests the presence of A-type apatite in all the samples. Osteoporotic and control samples show similar spectral behavior, except for sample OsteopS FN, which exhibited peculiar spectral signals in correspondence with the Amide II region. The above-mentioned signals in OsteopS FN might be due to multiple bands overlapping, including also the contribution of carboxylates (bands at 1540, 1570, and 1576 cm^{-1}), generated possibly by the interaction of calcium and fatty materials.

Some limitations have to be acknowledged, the first being the use of only two samples and second the synchrotron images focusing only on the FN of the two scanned proximal femurs. The synchrotron beamtime allowed us to fully explore and characterize only one bone region. Therefore, we decided to investigate the proximal femur region more exposed to fractures. A total of 14% of all the fragility fractures occur in the elderly, and are some of the most invalidating, and with high mortality risk (4.3% in-hospital death in patients with mean age of 79.5 years) [18]. Moreover, the two femurs have been accurately selected in order to have very different DXA-BMD, while being extremely alike (gender-, age- and heigh-matched). However, no differences in the OL shape have been assessed in the femoral neck, and as a future perspective we may suggest that it would be interesting to evaluate the OL characteristics also in the great trochanter and the femoral head. In the femoral neck, the differences in the bone mineralized phase suggested by microindentation could be investigated at the molecular scale, as well as for the hydroxyapatite structure, organization and composition.

5. Conclusions

In this study, the bone quality in a femoral neck has been characterized using a multiscale and multimodal approach of one osteoporotic subject and one gender- and age-matched control. The proposed method combined X-ray microtomography analyses with Fourier transform infrared spectroscopy and microindentation; this facilitated the investigation of bone quality from the macro scale, by assessing the whole proximal femur region, to the microscale with the assessment of the osteocyte lacunae morphology and organization, and from the trabeculae tissue properties to the molecular scale with the investigation of the mineralization and carbonate accumulation. Our results suggested that small differences could be associated with osteoporosis in the cortical bone phase, while the trabecular network resulted in a greater impact. Moreover, the analysis conducted at the microscale highlighted differences in the trabeculae mechanical properties between the osteoporotic and the healthy subject in both femoral head and great trochanter, while no differences were assessed in the femoral neck in both the mechanical properties and osteocytes lacunae shape and organization. These results suggested that healthy femoral neck was already impacted by an intensive bone remodeling process, and hence femoral neck is the first proximal femur region impacted by osteoporosis. Finally, the qualitative interpretation of FT-IR spectra showed comparable chemical bone composition between subregions. Although a larger study including more samples, both gender and multiple age ranges would be of great interest, this study clearly shows the interest of the bone microarchitecture assessment for evaluating patients' osteoporotic state.

Author Contributions: Conceptualization, J.V., M.P., D.B., S.I., E.M. and E.S.; methodology, J.V., M.P., D.B., S.I., E.M., E.S., L.M., S.P., G.S. and F.R.; software, J.V., E.S., F.R., L.M. and E.C.; validation, D.G., J.V., M.P., D.B., S.I., E.M. and L.M.; formal analysis, E.S., F.R. and E.C.; investigation, E.S., F.R. and E.C.; resources, D.G., J.V., M.P., D.B. and E.S.; data curation, E.S., F.R., E.C.; writing—original draft preparation, E.S.; writing—review and editing, J.V., M.P., D.B., S.I., E.M., E.S., L.M., F.R. and E.C.; visualization, J.V., M.P., D.B., S.I., E.M., E.S., L.M., F.R. and E.C.; supervision, J.V., M.P., D.B., S.I. and E.M.; project administration, J.V., M.P. and D.B.; funding acquisition, J.V., M.P. and D.B. All authors have read and agreed to the published version of the manuscript.

Funding: This project has received funding from the European Union's Horizon 2020 research and innovation program under the Marie Skodowska-Curie grant agreement No713750. Additionally, it has been carried out with the financial support of the Regional Council of Provence- Alpes-Côte d'Azur and with the financial support of the A*MIDEX (n ANR- 11-IDEX-0001-02), funded by the "Investissements d'Avenir" project funded by the French Government, managed by the French National Research Agency (ANR).

Institutional Review Board Statement: The study was conducted in accordance with the ethical standards of the responsible committee on human experimentation of the thanatopraxy laboratory, University School of Medicine, Hôpital de la Timone, Marseille, France that provided the bodies coming from body donation and in accordance with the Helsinki Declaration of 1975, as revised in 2000. The Aix-Marseille Ethics Committee (chaired by Pierre-JeanWeiller) judged that this project (N/ref dossier 2018-08-11-002) does not pose an ethical or regulatory problem.

Informed Consent Statement: Not applicable.

Data Availability Statement: The data presented in this study are available on request from the corresponding author. The data are not publicly available due to restrictions imposed by Aix Marseille University and by the local ethics committee regarding patients data sharing.

Conflicts of Interest: The authors declare no conflict of interest. The funders had no role in the design of the study; in the collection, analyses, or interpretation of data; in the writing of the manuscript, or in the decision to publish the results.

Appendix A. Femoral Neck Macroscale Analysis

The hierarchical bone quality has been investigated. The bone cortical characteristics have been compared between the osteoporotic subject and the control using μCT images. The trabecular characteristics have been compared using μCT and SRμCT singularly and between acquisition techniques evaluating the informative contribution by reducing the voxel size up to an order of magnitude.

Materials and Methods

Laboratory-based X-ray computed microtomography (μCT) scans of both the proximal femurs were acquired using a Rx-Solution EasyTom XL ULTRA microtomographic instrument [44], equipped with a X-ray Hamamatsu tube allowing a minimum focal spot size of 5 μm. To cover the whole femoral head, an isovolumetric voxel size of 0.051 mm has been chosen. The other parameters were: current = 343 μA current, Voltage = 150 kV, 8 images/s and 1440 projections over 360 degrees of total scan angle. Each projection was obtained from the average of 10 images to increase the signal to noise ratio. The acquisition lasted approximatively 40 min.

Image processing and analysis for laboratory- and synchrotron radiation (SR) microtomographic data

The total femoral neck volume acquired at a pixel size of 51.0×51.0 μm^2 (Figure 3b) has been first manually divided in two different VOIs, one keeping the cortical phase and one the trabecular phase. The binarization of both VOIs were straightforward as the contrast was high and the voxel size was smaller than the trabecular thickness and was performed by manually selecting the gray level value from the gray level distribution of the whole VOI that better separated the solid phase from the bone marrow. Based on binarized ROIs, it has been calculated the bone mineral content (BMC), derived from the total bone volume present in both the cortical and the trabecular ROI and multiplied by the bone tissue mineral density (ρ = 1.2 g/cm^3) [82,83]. Moreover, in the trabecular phase it has

been calculated the bone volume fraction (BVF), which refers to the ratio between the bone volume and the total volume, the trabecular thickness (Tb.Th) and spacing (Tb.Sp), which provide information about the trabecular diameters and distance between two trabeculae, respectively. In the cortical phase, it has been calculated the cortical thickness (Ct.Th) which refers to the thickness of the outer femoral neck shell. Tb.Th, Tb.Sp and Ct.Th have been extrapolated using the distance transformation map from which it has been derived the aperture map using the software iMorph [50,51]. The aperture map provides for every pixel of the bone the diameter of the maximal disk totally enclosed in the bone and containing this voxel. Tb.Th and Ct.Th were then deduced from the mean values of the aperture map distribution. Tb.Sp was quantified from similar computations in the marrow phase of the trabecular ROI. The aperture map has been previously used for the 3D morphological evaluation of porous materials in different fields [50,84,85] and provides local information with a sub-voxel precision [50,86]. The central femoral neck core acquired using the SRμCT at 4.95 μm^3 (Figure 3c), in which was present the trabecular phase only, followed the same image analysis the same bone characteristics were retrieved.

Macroscale Results

The image analysis conducted using μCT images at 51.0 μm of voxel size in the cortical ROI showed a similar average cortical thickness of the shell with the osteoporotic bone being 2% thinner than the control (0.72 ± 0.48 mm and 0.74 ± 0.52 mm, respectively for the osteoporotic and the control). Moreover, the morphological analysis performed on the ROI which include the whole trabecular phase of the femoral neck showed higher differences between the two subjects with the osteoporotic subject presenting lower BVF (−13%) and Tb.Th (−12%) and higher Tb.Sp (+8%) compared to the control (Table A1 and Figure A1). The analysis on the BMC of both the cortical and the trabecular ROI showed similar results comparing the osteoporotic to the control for the cortical ROI (3% higher BMC for the osteoporotic compared to the control, respectively 1.72 vs. 1.67 g/mm^3). However, this was not the case in the trabecular ROI, where the results showed that the BMC was +21% higher for the control than the osteoporotic (1.41 vs. 1.11 g/mm^3).

The morphology analysis performed in the central core of the femoral neck acquired using SRμCT at pixel size of 4.95 μm showed similar results (Table A1 and Figure A1). Although, the synchrotron-based μCT data showed mean values different from those derived by laboratory-based images, the Tb.Th and the BVF values obtained using SRμCT data being, respectively 35% and 56% lower and the Tb.Sp was 17% higher than those derived from laboratory μCT images, the trend between osteoporotic and control was comparable. In particular, the osteoporotic subject presented reduced Tb.Th (−5%) and BVF (−33%) and increased Tb.Sp (+28%) compared to the control.

Lastly, using the SRμCT acquisition at 4.95 μm of pixel size, it was possible to assess the smallest trabeculae in the analyzed ROI. Specifically, evaluating the aperture map distribution profile of the solid phase and considering 1 × 106 occurrence as a threshold to assess the minimum trabeculae expression, the osteoporotic subject presented a minimum trabecular thickness 9% smaller than the minimum Tb.Th depicted by the control sample (0.052 ± 0.005 mm vs. 0.057 ± 0.003 mm, respectively for the osteoporotic and the control).

Table A1. Morphological analysis of the whole femoral neck and its core for both the osteoporotic and control sample.

	Whole Femoral Neck (51.0 μm)				Femoral Neck Core (4.95 μm)			
	Ct.Th (mm)	**Tb.Th (mm)**	**Tb.Sp (mm)**	**BVF**	**Tb.Th (mm)**	**Tb.Sp (mm)**	**BVF**	**Min Tb.Th (mm)**
Control	0.74 ± 0.52	0.21 ± 0.10	1.03 ± 0.51	0.158	0.13 ± 0.06	1.10 ± 0.29	0.079	0.057 ± 0.003
OsteopS	0.73 ± 0.48	0.18 ± 0.11	1.11 ± 0.59	0.137	0.12 ± 0.06	1.41 ± 0.47	0.053	0.052 ± 0.005
Diff	−2%	−12%	8%	−13%	−5%	28%	−33%	−8%

Data are presented as mean ± SD. Ct.Th: cortical thickness; Tb.Th: trabecular thickness; Tb.Sp: trabecular spacing; BVF: bone volume fraction; min Tb.Th: minimum values of trabecular thickness.

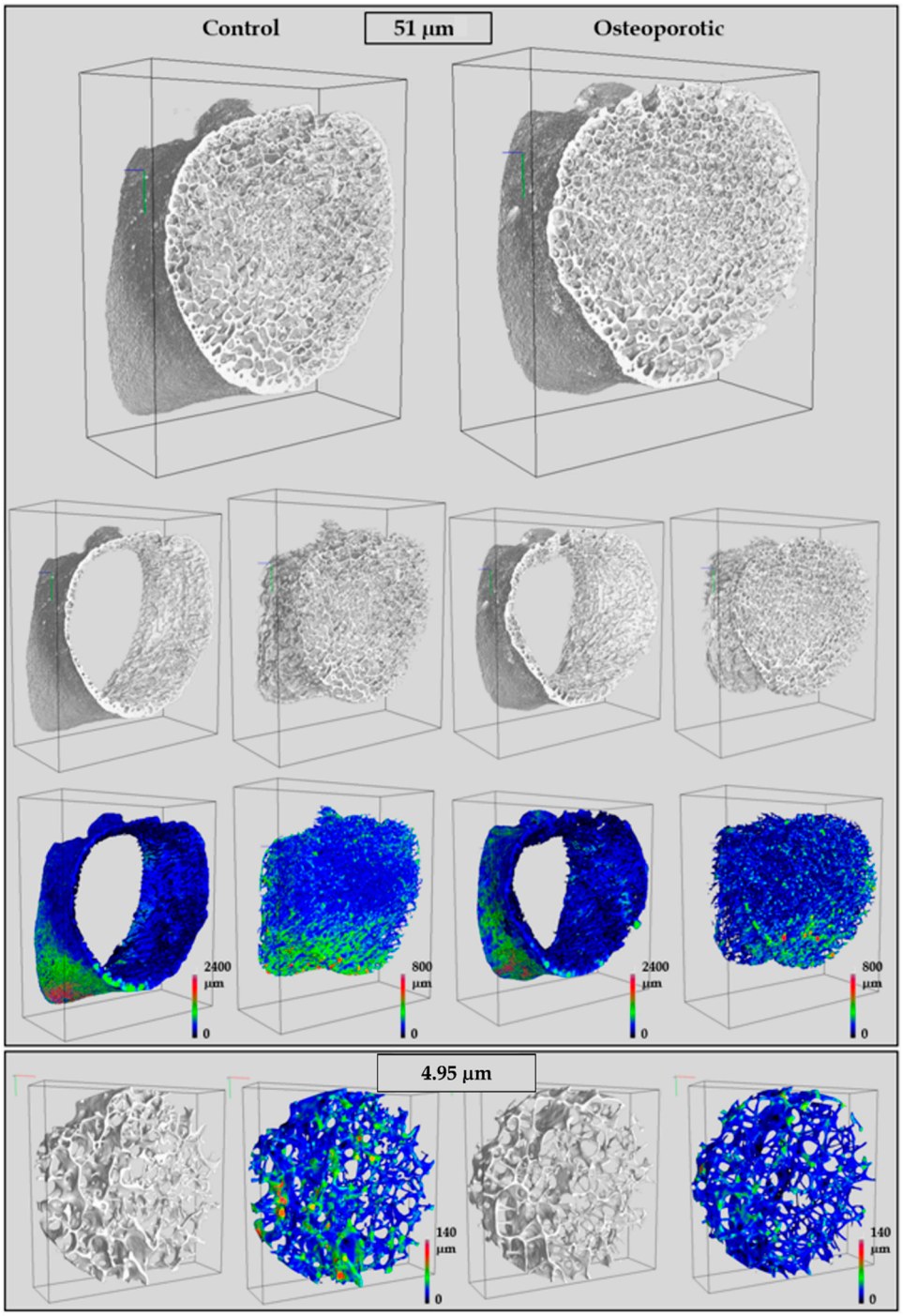

Figure A1. 3D morphology of the whole femoral neck acquired using µCT at 51.0 µm and its central core acquired using SRµCT at 4.95 µm of both the control and the osteoporotic subject.

Macroscale Discussion

The analysis conducted using µCT images acquired at a pixel size of 51.0 µm showed no difference in the cortical thickness and BMC between the osteoporotic and the control, however reporting differences in both the morphology and BMC in the trabecular phase. Similar bone morphology was assessed by Tjong et al. on a study conducted on 17 cadaveric radii scanned using µCT at 18 µm [87]. In their study, they reported a mean Ct.Th of 0.59 ± 0.19 mm, Tb.Th of 0.17 ± 0.01 mm and Tb.Sp of 0.75 ± 0.15 mm, where the differences for both Ct.Th and Tb.Sp could be explained by the different anatomical site. Moreover, in a study conducted on 34 femoral neck (11 affected by rheumatoid arthri-

tis, 15 affected by osteoarthritis and 8 controls), harvested during total hip replacement and scanned using μCT at 19 μm, Wang et al. reported that morphological parameters (Ct.Th = 0.64 ± 0.2 mm, Tb.Th = 0.18 ± 0.03 mm, BVF = 0.15 ± 0.09 and Tb.Sp = 0.93 ± 0.32 mm) in the same range of those reported in this study [88]. However, Wang et al. reported that the patients showed greater Tb.Th and BVF and reduced Tb.Sp compared to controls [88]. This opposite effect could be explained by the different bone disease (rheumatoid arthritis and osteoarthritis vs. osteoporosis in our case). This hypothesis was further supported by Li et al., where on a study conducted on 60 postmenopausal women (30 affected by osteoarthritis and 30 affected by osteoporosis) scanned in the femoral head using μCT at 36 μm, reported that osteoporotic patients showed reduced BVF, trabecular thinning and increased Tb.Sp [89].

Focusing in the central core of the femoral neck using SRμCT at 4.95 μm the trabecular morphology provided lower Tb.Th and BVF and higher Tb.Sp than those previously reported using μCT images at 51.0 μm. Although, those results were expected as the femoral neck is a highly in-homogeneous bone region with the solid phase progressively reducing its volume as approaching the central core, it was not expected to individuate greater discrepancies between the osteoporotic bone morphology and the control than those derived from the whole femoral necks. This result may suggest that the bone remodeling is not uniform and that works at different rate at different regions. Juan et al. on a study conducted on 5 different anatomic regions of both distal femurs of 10 postmenopausal women scanned using the peripheric clinical CT scanner, i.e., high-resolution peripheral quantitative computed tomography (HRpQCT), with an isotropic voxel size of 82 μm, reported significant regional variation in the trabecular architecture ($0.001 < p < 0.05$) with differences up to 106% between lowest (central) and highest (medial and posterior) regions [90]. Local differences in the trabecular bone architecture were also been assessed in different anatomical sites, as for the calcaneus [91], the glenoid [92] and the proximal femur [93] but not extensively investigated in the femoral neck, which is an osteoporotic fracture site and one of the most invalidating [94]. One could suggest that reducing the voxel size would allow a better characterization of the thinnest solid structures, however our results suggest that the bone morphology was already correctly characterized at 51.0 μm. In addition, using the μCT acquisition at 51.0 μm it was possible to visualize the whole proximal femur in approximately 40 min therefore providing a more complete overview of the bone quality also allowing the characterization of both the cortical and the trabecular phase. SRμCT images at 4.95 μm allowed the characterization of the smallest trabeculae present in the central femoral core reporting a minimum trabecular thickness of 50 μm and therefore suggesting that the bone morphology would be completely resolved using a voxel size in range 15–25 μm. These voxel dimensions would completely resolve both cortical and trabecular phase of the whole proximal femur in 2 to 3 acquisitions. In fact, using a voxel size of 25 μm or 15 μm the field of view would be, respectively of 5.1 cm and 3.1 cm which would allow the acquisition of the great trochanter, the femoral neck and head in, respectively 2 or 3 scans.

Appendix B. Image Processing Effect on OL Characterization

We also investigated the possible effect of our image pre-processing. First, the pore regions distribution has been investigated to evaluate the classification efficacy between noise (pores volume < 73 μm^3), OL (pores volume between 73 and 1000 μm^3) and vessels (pores volume > 1000 μm^3). The pore region distribution reported in Figure A2 showed that the range selected for the OL classification is coherent and allowed the separation between the three phases, and therefore could be used in further studies. Moreover, the OL image analysis described in the previous section has been performed on the same VOI choosing two different thresholds (+ 5 and −5% of the best manually identified threshold) and by comparing the effect of the 3D median filter (kernel size 3 × 3 × 3 pixels) applied before performing the image analysis. The results of OL characteristics after the application of different thresholds showed errors in the same +5/−5% range. The committed maximum

error in the number of individuated OL was −4% reducing the threshold of 5% and +4% when the threshold was increased. Similar results were assessed for the OL volume (−6% and +5%, respectively for reduced and increased thresholds), surface (−4% and +4%, respectively) and region of action (+6% and −5%). Regarding the OL shape the differences were even lower with a maximum error of +2% in the principal axes and +1% in the aspect ratios, sphericity and fractal anisotropy for reduced thresholds of 5% and −3% in the principal axes and −1% in the aspect ratios, sphericity and fractal anisotropy for thresholds increased by 5%.

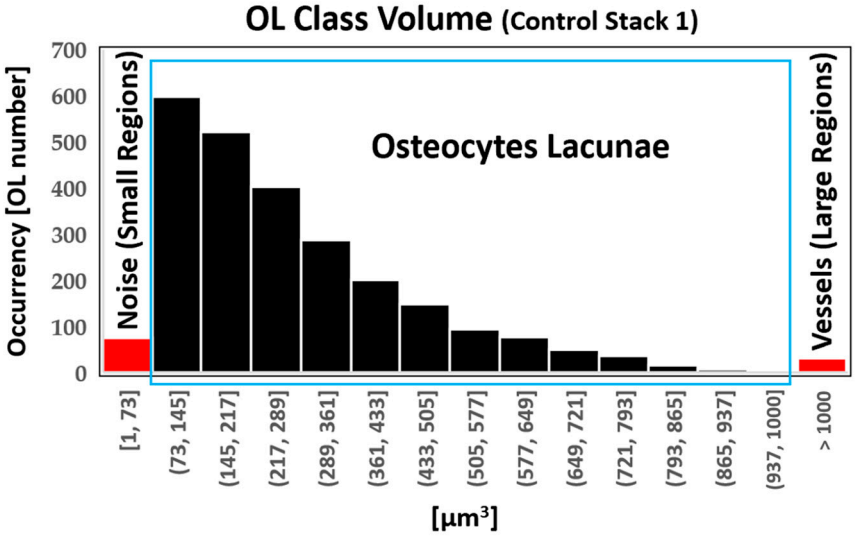

Figure A2. Distribution of the individuated Osteocytes lacunae (OL) in the bone solid phase. Red bar shows the objects smaller than 73 µm^3 classified as noise (objects smaller than 27 voxels that have been re-added to the solid phase) and small pores (objects within 28 and 100 voxels not classified as OL), and the objects bigger than 1000 µm^3 classified as blood vessels. The light blue square indicates the objects classified as OL.

The investigation of the pre-processing steps was necessary to evaluate the robustness of our analysis since the stack of images have been segmented using a threshold manually selected and the investigation was focusing on very small objects that could have been lost during the pre-processing. The analysis conducted applying two different thresholds (+5 and −5%) from the best manually individuated, demonstrated that the committed errors were small, and the OL characteristics were comparable (maximum committed error in OL shape was in range +3 and −3%, therefore proving the robustness of our approach and the high image quality. Moreover, the application of the median filter showed that the OL volume uniformly increased by 6% compared to the original one, while no difference was assessed in the OL shape, sphericity nor fractal anisotropy. The median filter is usually applied to reduce the "salt and pepper" noise and it has been showed previously that median pre-filtering improves the thresholding performance while preserving the image edges [95].

References

1. Tresguerres, F.G.F.; Torres, J.; López-Quiles, J.; Hernández, G.; Vega, J.A.; Tresguerres, I.F. The osteocyte: A multifunctional cell within the bone. *Ann. Anat.—Anat. Anz.* **2020**, *227*, 151422. [CrossRef] [PubMed]
2. Hinton, P.V.; Rackard, S.M.; Kennedy, O.D. In Vivo Osteocyte Mechanotransduction: Recent Developments and Future Directions. *Curr. Osteoporos. Rep.* **2018**, *16*, 746–753. [CrossRef] [PubMed]
3. Yavropoulou, M.P.; Yovos, J.G. The molecular basis of bone mechanotransduction. *J. Musculoskelet. Neuronal. Interact.* **2016**, *16*, 221–236. [PubMed]
4. van Oers, R.F.M.; Wang, H.; Bacabac, R.G. Osteocyte Shape and Mechanical Loading. *Curr. Osteoporos. Rep.* **2015**, *13*, 61–66. [CrossRef] [PubMed]
5. Knothe Tate, M.L.; Adamson, J.R.; Tami, A.E.; Bauer, T.W. The osteocyte. *Int. J. Biochem. Cell Biol.* **2004**, *36*, 1–8. [CrossRef]

6. Qiu, S.; Rao, D.S.; Palnitkar, S.; Parfitt, A.M. Differences in osteocyte and lacunar density between Black and White American women. *Bone* **2006**, *38*, 130–135. [CrossRef]
7. Sasaki, M.; Kuroshima, S.; Aoki, Y.; Inaba, N.; Sawase, T. Ultrastructural alterations of osteocyte morphology via loaded implants in rabbit tibiae. *J. Biomech.* **2015**, *48*, 4130–4141. [CrossRef]
8. Katsamenis, O.L.; Chong, H.M.H.; Andriotis, O.G.; Thurner, P.J. Load-bearing in cortical bone microstructure: Selective stiffening and heterogeneous strain distribution at the lamellar level. *J. Mech. Behav. Biomed. Mater.* **2013**, *17*, 152–165. [CrossRef]
9. Ashique, A.M.; Hart, L.S.; Thomas, C.D.L.; Clement, J.G.; Pivonka, P.; Carter, Y.; Mousseau, D.D.; Cooper, D.M.L. Lacunar-canalicular network in femoral cortical bone is reduced in aged women and is predominantly due to a loss of canalicular porosity. *Bone Rep.* **2017**, *7*, 9–16. [CrossRef]
10. Hasegawa, T.; Yamamoto, T.; Hongo, H.; Qiu, Z.; Abe, M.; Kanesaki, T.; Tanaka, K.; Endo, T.; de Freitas, P.H.L.; Li, M.; et al. Three-dimensional ultrastructure of osteocytes assessed by focused ion beam-scanning electron microscopy (FIB-SEM). *Histochem. Cell Biol.* **2018**, *149*, 423–432. [CrossRef]
11. Genthial, R.; Beaurepaire, E.; Schanne-Klein, M.-C.; Peyrin, F.; Farlay, D.; Olivier, C.; Bala, Y.; Boivin, G.; Vial, J.-C.; Débarre, D.; et al. Label-free imaging of bone multiscale porosity and interfaces using third-harmonic generation microscopy. *Sci. Rep.* **2017**, *7*, 3419. [CrossRef] [PubMed]
12. Kamel-ElSayed, S.A.; Tiede-Lewis, L.M.; Lu, Y.; Veno, P.A.; Dallas, S.L. Novel approaches for two and three dimensional multiplexed imaging of osteocytes. *Bone* **2015**, *76*, 129–140. [CrossRef] [PubMed]
13. Yu, B.; Pacureanu, A.; Olivier, C.; Cloetens, P.; Peyrin, F. Assessment of the human bone lacuno-canalicular network at the nanoscale and impact of spatial resolution. *Sci. Rep.* **2020**, *10*, 4567. [CrossRef]
14. Dong, P.; Haupert, S.; Hesse, B.; Langer, M.; Gouttenoire, P.-J.; Bousson, V.; Peyrin, F. 3D osteocyte lacunar morphometric properties and distributions in human femoral cortical bone using synchrotron radiation micro-CT images. *Bone* **2014**, *60*, 172–185. [CrossRef] [PubMed]
15. Carter, Y.; Thomas, C.D.L.; Clement, J.G.; Peele, A.G.; Hannah, K.; Cooper, D.M.L. Variation in osteocyte lacunar morphology and density in the human femur—A synchrotron radiation micro-CT study. *Bone* **2013**, *52*, 126–132. [CrossRef]
16. Suuronen, J.-P.; Hesse, B.; Langer, M.; Bohner, M.; Villanova, J. Evaluation of imaging setups for quantitative phase contrast nanoCT of mineralized biomaterials. *J. Synchrotron Rad.* **2022**, *29*, 843–852. [CrossRef]
17. Van Hove, R.P.; Nolte, P.A.; Vatsa, A.; Semeins, C.M.; Salmon, P.L.; Smit, T.H.; Klein-Nulend, J. Osteocyte morphology in human tibiae of different bone pathologies with different bone mineral density—Is there a role for mechanosensing? *Bone* **2009**, *45*, 321–329. [CrossRef]
18. Bouyer, B.; Leroy, F.; Rudant, J.; Weill, A.; Coste, J. Burden of fractures in France: Incidence and severity by age, gender, and site in 2016. *Int. Orthop.* **2020**, *44*, 947–955. [CrossRef]
19. Soldati, E.; Rossi, F.; Vicente, J.; Guenoun, D.; Pithioux, M.; Iotti, S.; Malucelli, E.; Bendahan, D. Survey of MRI Usefulness for the Clinical Assessment of Bone Microstructure. *IJMS* **2021**, *22*, 2509. [CrossRef]
20. Chang, G.; Boone, S.; Martel, D.; Rajapakse, C.S.; Hallyburton, R.S.; Valko, M.; Honig, S.; Regatte, R.R. MRI assessment of bone structure and microarchitecture: Bone Structure and Microarchitecture. *J. Magn. Reson. Imaging* **2017**, *46*, 323–337. [CrossRef]
21. Soldati, E.; Pithioux, M.; Guenoun, D.; Bendahan, D.; Vicente, J. Assessment of Bone Microarchitecture in Fresh Cadaveric Human Femurs: What Could Be the Clinical Relevance of Ultra-High Field MRI. *Diagnostics* **2022**, *12*, 439. [CrossRef] [PubMed]
22. Alford, A.I.; Kozloff, K.M.; Hankenson, K.D. Extracellular matrix networks in bone remodeling. *Int. J. Biochem. Cell Biol.* **2015**, *65*, 20–31. [CrossRef] [PubMed]
23. Wu, D.; Isaksson, P.; Ferguson, S.J.; Persson, C. Young's modulus of trabecular bone at the tissue level: A review. *Acta Biomater.* **2018**, *78*, 1–12. [CrossRef] [PubMed]
24. Boskey, A.L. Matrix Proteins and Mineralization: An Overview. *Connect. Tissue Res.* **1996**, *35*, 357–363. [CrossRef]
25. Gong, B.; Mandair, G.S.; Wehrli, F.W.; Morris, M.D. Novel Assessment Tools for Osteoporosis Diagnosis and Treatment. *Curr. Osteoporos. Rep.* **2014**, *12*, 357–365. [CrossRef]
26. Pérez-Sáez, M.J.; Herrera, S.; Prieto-Alhambra, D.; Nogués, X.; Vera, M.; Redondo-Pachón, D.; Mir, M.; Güerri, R.; Crespo, M.; Díez-Pérez, A.; et al. Bone Density, Microarchitecture, and Tissue Quality Long-term After Kidney Transplant. *Transplantation* **2017**, *101*, 1290–1294. [CrossRef]
27. Soldado-Folgado, J.; Lerma-Chippirraz, E.; Arrieta-Aldea, I.; Bujosa, D.; García-Giralt, N.; Pineda-Moncusi, M.; Trenchs-Rodríguez, M.; Villar-García, J.; González-Mena, A.; Díez-Pérez, A.; et al. Bone density, microarchitecture and tissue quality after 1 year of treatment with dolutegravir/abacavir/lamivudine. *J. Antimicrob. Chemother.* **2020**, *75*, 2998–3003. [CrossRef]
28. Ovejero Crespo, D. Microindentation: A New Technique for Bone Quality Assessment. *Adv. Ther.* **2020**, *37*, 47–54. [CrossRef]
29. Diez-Perez, A.; Güerri, R.; Nogues, X.; Cáceres, E.; Peña, M.J.; Mellibovsky, L.; Randall, C.; Bridges, D.; Weaver, J.C.; Proctor, A.; et al. Microindentation for in vivo measurement of bone tissue mechanical properties in humans. *J. Bone Miner. Res.* **2010**, *25*, 1877–1885. [CrossRef]
30. Greenwood, C.; Clement, J.; Dicken, A.; Evans, J.P.O.; Lyburn, I.; Martin, R.M.; Rogers, K.; Stone, N.; Zioupos, P. Towards new material biomarkers for fracture risk. *Bone* **2016**, *93*, 55–63. [CrossRef]
31. Keen, C.E.; Whittier, D.E.; Firminger, C.R.; Edwards, W.B.; Boyd, S.K. Validation of Bone Density and Microarchitecture Measurements of the Load-Bearing Femur in the Human Knee Obtained Using In Vivo HR-pQCT Protocol. *J. Clin. Densitom.* **2021**, *24*, 651–657. [CrossRef] [PubMed]

32. Von Euw, S.; Wang, Y.; Laurent, G.; Drouet, C.; Babonneau, F.; Nassif, N.; Azaïs, T. Bone mineral: New insights into its chemical composition. *Sci. Rep.* **2019**, *9*, 8456. [CrossRef] [PubMed]
33. Paschalis, E.P.; Gamsjaeger, S.; Klaushofer, K. Vibrational spectroscopic techniques to assess bone quality. *Osteoporos. Int.* **2017**, *28*, 2275–2291. [CrossRef] [PubMed]
34. Garcia, I.; Chiodo, V.; Ma, Y.; Boskey, A. Evidence of altered matrix composition in iliac crest biopsies from patients with idiopathic juvenile osteoporosis. *Connect. Tissue Res.* **2016**, *57*, 28–37. [CrossRef]
35. Boskey, A.L.; Donnelly, E.; Boskey, E.; Spevak, L.; Ma, Y.; Zhang, W.; Lappe, J.; Recker, R.R. Examining the Relationships Between Bone Tissue Composition, Compositional Heterogeneity, and Fragility Fracture: A Matched Case-Controlled FTIRI Study: Association of Ftiri Variables and Fragility Fractures. *J. Bone Miner. Res.* **2016**, *31*, 1070–1081. [CrossRef]
36. Jin, Y.; Zhang, T.; Lui, Y.F.; Sze, K.Y.; Lu, W.W. The measured mechanical properties of osteoporotic trabecular bone decline with the increment of deformation volume during micro-indentation. *J. Mech. Behav. Biomed. Mater.* **2020**, *103*, 103546. [CrossRef] [PubMed]
37. Jadzic, J.; Milovanovic, P.; Cvetkovic, D.; Ivovic, M.; Tomanovic, N.; Bracanovic, M.; Zivkovic, V.; Nikolic, S.; Djuric, M.; Djonic, D. Mechano-structural alteration in proximal femora of individuals with alcoholic liver disease: Implications for increased bone fragility. *Bone* **2021**, *150*, 116020. [CrossRef]
38. O'Leary, T.J.; Rice, H.M.; Greeves, J.P. Biomechanical Basis of Predicting and Preventing Lower Limb Stress Fractures During Arduous Training. *Curr. Osteoporos. Rep.* **2021**, *19*, 308–317. [CrossRef]
39. McCreadie, B.R.; Hollister, S.J.; Schaffler, M.B.; Goldstein, S.A. Osteocyte lacuna size and shape in women with and without osteoporotic fracture. *J. Biomech.* **2004**, *37*, 563–572. [CrossRef]
40. Kollmannsberger, P.; Kerschnitzki, M.; Repp, F.; Wagermaier, W.; Weinkamer, R.; Fratzl, P. The small world of osteocytes: Connectomics of the lacuno-canalicular network in bone. *New J. Phys.* **2017**, *19*, 073019. [CrossRef]
41. Rolvien, T.; Milovanovic, P.; Schmidt, F.N.; Kroge, S.; Wölfel, E.M.; Krause, M.; Wulff, B.; Püschel, K.; Ritchie, R.O.; Amling, M.; et al. Long-Term Immobilization in Elderly Females Causes a Specific Pattern of Cortical Bone and Osteocyte Deterioration Different From Postmenopausal Osteoporosis. *J. Bone Miner. Res.* **2020**, *35*, 1343–1351. [CrossRef] [PubMed]
42. Renault, J.-B.; Carmona, M.; Tzioupis, C.; Ollivier, M.; Argenson, J.-N.; Parratte, S.; Chabrand, P. Tibial subchondral trabecular bone micromechanical and microarchitectural properties are affected by alignment and osteoarthritis stage. *Sci. Rep.* **2020**, *10*, 3975. [CrossRef] [PubMed]
43. Gustafson, M.B.; Martin, R.B.; Gibson, V.; Storms, D.H.; Stover, S.M.; Gibeling, J.; Griffin, L. Calcium buffering is required to maintain bone stiffness in saline solution. *J. Biomech.* **1996**, *29*, 1191–1194. [CrossRef]
44. RX Solutions SAS, 3D X-ray Tomography Systems. Available online: http://www.3d-skenovani.cz/wp-content/uploads/2021/05/2021_RX_SOLUTIONS_CT_SERIE.pdf (accessed on 29 September 2022).
45. Soldati, E.; Vicente, J.; Guenoun, D.; Bendahan, D.; Pithioux, M. Validation and Optimization of Proximal Femurs Microstructure Analysis Using High Field and Ultra-High Field MRI. *Diagnostics* **2021**, *11*, 1603. [CrossRef]
46. Brun, F.; Pacilè, S.; Accardo, A.; Kourousias, G.; Dreossi, D.; Mancini, L.; Tromba, G.; Pugliese, R. Enhanced and Flexible Software Tools for X-ray Computed Tomography at the Italian Synchrotron Radiation Facility Elettra. *Fundam. Inform.* **2015**, *141*, 233–243. [CrossRef]
47. van Aarle, W.; Palenstijn, W.J.; De Beenhouwer, J.; Altantzis, T.; Bals, S.; Batenburg, K.J.; Sijbers, J. The ASTRA Toolbox: A platform for advanced algorithm development in electron tomography. *Ultramicroscopy* **2015**, *157*, 35–47. [CrossRef]
48. Baker, D.R.; Mancini, L.; Polacci, M.; Higgins, M.D.; Gualda, G.A.R.; Hill, R.J.; Rivers, M.L. An introduction to the application of X-ray microtomography to the three-dimensional study of igneous rocks. *Lithos* **2012**, *148*, 262–276. [CrossRef]
49. Paganin, D.; Mayo, S.C.; Gureyev, T.E.; Miller, P.R.; Wilkins, S.W. Simultaneous phase and amplitude extraction from a single defocused image of a homogeneous object. *J. Microsc.* **2002**, *206*, 33–40. [CrossRef]
50. Brun, E.; Ferrero, C.; Vicente, J. Fast Granulometry Operator for the 3D Identification of Cell Structures. *Fundam. Inform.* **2017**, *155*, 363–372. [CrossRef]
51. Brun, E.; Vicente, J.; Topin, F.; Occelli, R. iMorph: A 3D morphological tool to fully analyze all kind of cellular materials. *Cell. Met. Struct. Funct. Appl.* **2008**, *6*.
52. Benouali, A.-H.; Froyen, L.; Dillard, T.; Forest, S.; N'guyen, F. Investigation on the influence of cell shape anisotropy on the mechanical performance of closed cell aluminium foams using micro-computed tomography. *J. Mater. Sci.* **2005**, *40*, 5801–5811. [CrossRef]
53. Özarslan, E.; Vemuri, B.C.; Mareci, T.H. Generalized scalar measures for diffusion MRI using trace, variance, and entropy: Generalized Scalar Measures for Diffusion MRI. *Magn. Reson. Med.* **2005**, *53*, 866–876. [CrossRef] [PubMed]
54. Oliver, W.C.; Pharr, G.M. An improved technique for determining hardness and elastic modulus using load and displacement sensing indentation experiments. *J. Mater. Res.* **1992**, *7*, 1564–1583. [CrossRef]
55. Zysset, P.K. Indentation of bone tissue: A short review. *Osteoporos. Int.* **2009**, *20*, 1049–1055. [CrossRef] [PubMed]
56. Ren, F.; Ding, Y.; Leng, Y. Infrared spectroscopic characterization of carbonated apatite: A combined experimental and computational study: Ir Spectroscopic Characterization of CAp. *J. Biomed. Mater. Res.* **2014**, *102*, 496–505. [CrossRef]
57. Rehman, I.; Bonfield, W. Characterization of hydroxyapatite and carbonated apatite by photo acoustic FTIR spectroscopy. *J. Mater. Sci. Mater. Med.* **1997**, *8*, 1–4. [CrossRef]

58. Nesseri, E.; Boyatzis, S.C.; Boukos, N.; Panagiaris, G. Optimizing the biomimetic synthesis of hydroxyapatite for the consolidation of bone using diammonium phosphate, simulated body fluid, and gelatin. *SN Appl. Sci.* **2020**, *2*, 1892. [CrossRef]
59. Elliott, J.C. Synthetic and Biological Carbonate Apatites and Other Calcium Orthophosphates. In *Studies in Inorganic Chemistry*; Elsevier: Amsterdam, The Netherlands, 1994; Volume 18, ISBN 978-1-4832-9031-7.
60. Paschalis, E.P. Fourier Transform Infrared Imaging of Bone. In *Bone Research Protocols*; Idris, A.I., Ed.; Methods in Molecular Biology; Springer: New York, NY, USA, 2019; Volume 1914, pp. 641–649. Available online: http://link.springer.com/10.1007/978-1-4939-8997-3_34 (accessed on 29 October 2022)ISBN 978-1-4939-8996-6.
61. Schmidt, F.N.; Zimmermann, E.A.; Campbell, G.M.; Sroga, G.E.; Püschel, K.; Amling, M.; Tang, S.Y.; Vashishth, D.; Busse, B. Assessment of collagen quality associated with non-enzymatic cross-links in human bone using Fourier-transform infrared imaging. *Bone* **2017**, *97*, 243–251. [CrossRef]
62. Zhai, M.; Lu, Y.; Fu, J.; Zhu, Y.; Zhao, Y.; Shang, L.; Yin, J. Fourier transform infrared spectroscopy research on subchondral bone in osteoarthritis. *Spectrochim. Acta Part A Mol. Biomol. Spectrosc.* **2019**, *218*, 243–247. [CrossRef]
63. Ren, F.Z.; Leng, Y. Carbonated Apatite, Type-A or Type-B? *KEM* **2011**, *493–494*, 293–297. [CrossRef]
64. Madupalli, H.; Pavan, B.; Tecklenburg, M.M.J. Carbonate substitution in the mineral component of bone: Discriminating the structural changes, simultaneously imposed by carbonate in A and B sites of apatite. *J. Solid State Chem.* **2017**, *255*, 27–35. [CrossRef] [PubMed]
65. Ortali, C.; Julien, I.; Vandenhende, M.; Drouet, C.; Champion, E. Consolidation of bone-like apatite bioceramics by spark plasma sintering of amorphous carbonated calcium phosphate at very low temperature. *J. Eur. Ceram. Soc.* **2018**, *38*, 2098–2109. [CrossRef]
66. Pedrosa, M.; Ferreira, M.T.; Batista de Carvalho, L.A.E.; Marques, M.P.M.; Curate, F. The association of osteochemometrics and bone mineral density in humans. *Am. J. Phys. Anthropol.* **2021**, *176*, 434–444. [CrossRef] [PubMed]
67. Fleet, M.E.; Liu, X.; King, P.L. Accommodation of the carbonate ion in apatite: An FTIR and X-ray structure study of crystals synthesized at 2–4 GPa. *Am. Mineral.* **2004**, *89*, 1422–1432. [CrossRef]
68. Stepien, K.R.; Yoder, C.H. Europium-Doped Carbonated Apatites. *Minerals* **2022**, *12*, 503. [CrossRef]
69. Figueiredo, M.; Fernando, A.; Martins, G.; Freitas, J.; Judas, F.; Figueiredo, H. Effect of the calcination temperature on the composition and microstructure of hydroxyapatite derived from human and animal bone. *Ceram. Int.* **2010**, *36*, 2383–2393. [CrossRef]
70. Rey, C.; Collins, B.; Goehl, T.; Dickson, I.R.; Glimcher, M.J. The carbonate environment in bone mineral: A resolution-enhanced fourier transform infrared spectroscopy study. *Calcif Tissue Int.* **1989**, *45*, 157–164. [CrossRef]
71. Sotiropoulou, S.; Sciutto, G.; Tenorio, A.L.; Mazurek, J.; Bonaduce, I.; Prati, S.; Mazzeo, R.; Schilling, M.; Colombini, M.P. Advanced analytical investigation on degradation markers in wall paintings. *Microchem. J.* **2018**, *139*, 278–294. [CrossRef]
72. Magni, P.A.; Lawn, J.; Guareschi, E.E. A practical review of adipocere: Key findings, case studies and operational considerations from crime scene to autopsy. *J. Forensic Leg. Med.* **2021**, *78*, 102109. [CrossRef]
73. Ammarullah, M.I.; Santoso, G.; Sugiharto, S.; Supriyono, T.; Kurdi, O.; Tauviqirrahman, M.; Winarni, T.I.; Jamari, J. Tresca stress study of CoCrMo-on-CoCrMo bearings based on body mass index using 2D computational model. *Tribol. J.* **2022**, *33*, 31–38.
74. Zysset, P.K.; Edward Guo, X.; Edward Hoffler, C.; Moore, K.E.; Goldstein, S.A. Elastic modulus and hardness of cortical and trabecular bone lamellae measured by nanoindentation in the human femur. *J. Biomech.* **1999**, *32*, 1005–1012. [CrossRef]
75. Hengsberger, S.; Kulik, A.; Zysset, P. Nanoindentation discriminates the elastic properties of individual human bone lamellae under dry and physiological conditions. *Bone* **2002**, *30*, 178–184. [CrossRef]
76. Hoffler, C.E.; Moore, K.E.; Kozloff, K.; Zysset, P.K.; Brown, M.B.; Goldstein, S.A. Heterogeneity of bone lamellar-level elastic moduli. *Bone* **2000**, *26*, 603–609. [CrossRef]
77. Kokot, G.; Makuch, A.; Skalski, K.; Bańczerowski, J. Mechanical properties of cancellous tissue in compression test and nanoindentation. *BME* **2018**, *29*, 415–426. [CrossRef]
78. Pawlikowski, M.; Skalski, K.; Bańczerowski, J.; Makuch, A.; Jankowski, K. Stress–strain characteristic of human trabecular bone based on depth sensing indentation measurements. *Biocybern. Biomed. Eng.* **2017**, *37*, 272–280. [CrossRef]
79. Fratzl-Zelman, N.; Roschger, P.; Gourrier, A.; Weber, M.; Misof, B.M.; Loveridge, N.; Reeve, J.; Klaushofer, K.; Fratzl, P. Combination of Nanoindentation and Quantitative Backscattered Electron Imaging Revealed Altered Bone Material Properties Associated with Femoral Neck Fragility. *Calcif. Tissue Int.* **2009**, *85*, 335–343. [CrossRef]
80. Dall'Ara, E.; Karl, C.; Mazza, G.; Franzoso, G.; Vena, P.; Pretterklieber, M.; Pahr, D.; Zysset, P. Tissue properties of the human vertebral body sub-structures evaluated by means of microindentation. *J. Mech. Behav. Biomed. Mater.* **2013**, *25*, 23–32. [CrossRef]
81. Milovanovic, P.; Potocnik, J.; Djonic, D.; Nikolic, S.; Zivkovic, V.; Djuric, M.; Rakocevic, Z. Age-related deterioration in trabecular bone mechanical properties at material level: Nanoindentation study of the femoral neck in women by using AFM. *Exp. Gerontol.* **2012**, *47*, 154–159. [CrossRef]
82. Laval-Jeantet, A.-M.; Bergot, C.; Carroll, R.; Garcia-Schaefer, F. Cortical bone senescence and mineral bone density of the humerus. *Calcif. Tissue Int.* **1983**, *35*, 268–272. [CrossRef]
83. Tassani, S.; Öhman, C.; Baruffaldi, F.; Baleani, M.; Viceconti, M. Volume to density relation in adult human bone tissue. *J. Biomech.* **2011**, *44*, 103–108. [CrossRef]
84. Burghardt, A.J.; Link, T.M.; Majumdar, S. High-resolution Computed Tomography for Clinical Imaging of Bone Microarchitecture. *Clin. Orthop. Relat. Res.* **2011**, *469*, 2179–2193. [CrossRef] [PubMed]

85. Soldati, E.; Escoffier, L.; Gabriel, S.; Ogier, A.C.; Chagnaud, C.; Mattei, J.P.; Cammilleri, S.; Bendahan, D.; Guis, S. Assessment of in vivo bone microarchitecture changes in an anti-TNFα treated psoriatic arthritic patient. *PLoS ONE* **2021**, *16*, e0251788. [CrossRef] [PubMed]
86. Johansson, M.V.; Testa, F.; Perrier, P.; Vicente, J.; Bonnet, J.P.; Moulin, P.; Graur, I. Determination of an effective pore dimension for microporous media. *Int. J. Heat Mass Transf.* **2019**, *142*, 118412. [CrossRef]
87. Tjong, W.; Kazakia, G.J.; Burghardt, A.J.; Majumdar, S. The effect of voxel size on high-resolution peripheral computed tomography measurements of trabecular and cortical bone microstructure: HR-pQCT voxel size effects on bone microstructural measurements. *Med. Phys.* **2012**, *39*, 1893–1903. [CrossRef] [PubMed]
88. Wang, B.; Overgaard, S.; Chemnitz, J.; Ding, M. Cancellous and Cortical Bone Microarchitectures of Femoral Neck in Rheumatoid Arthritis and Osteoarthritis Compared with Donor Controls. *Calcif. Tissue Int.* **2016**, *98*, 456–464. [CrossRef]
89. Li, Z.-C.; Dai, L.-Y.; Jiang, L.-S.; Qiu, S. Difference in subchondral cancellous bone between postmenopausal women with hip osteoarthritis and osteoporotic fracture: Implication for fatigue microdamage, bone microarchitecture, and biomechanical properties. *Arthritis Rheum.* **2012**, *64*, 3955–3962. [CrossRef] [PubMed]
90. Du, J.; Brooke-Wavell, K.; Paggiosi, M.A.; Hartley, C.; Walsh, J.S.; Silberschmidt, V.V.; Li, S. Characterising variability and regional correlations of microstructure and mechanical competence of human tibial trabecular bone: An in-vivo HR-pQCT study. *Bone* **2019**, *121*, 139–148. [CrossRef]
91. Souzanchi, M.F.; Palacio-Mancheno, P.; Borisov, Y.A.; Cardoso, L.; Cowin, S.C. Microarchitecture and bone quality in the human calcaneus: Local variations of fabric anisotropy. *J. Bone Miner. Res.* **2012**, *27*, 2562–2572. [CrossRef]
92. Jun, B.-J.; Vasanji, A.; Ricchetti, E.T.; Rodriguez, E.; Subhas, N.; Li, Z.-M.; Iannotti, J.P. Quantification of regional variations in glenoid trabecular bone architecture and mineralization using clinical computed tomography images: Glenoid Trabecular Bone Architectural Variations. *J. Orthop. Res.* **2017**. Available online: https://onlinelibrary.wiley.com/doi/10.1002/jor.23620 (accessed on 9 July 2021). [CrossRef]
93. Issever, A.S.; Vieth, V.; Lotter, A.; Meier, N.; Laib, A.; Newitt, D.; Majumdar, S.; Link, T.M. Local Differences in the Trabecular Bone Structure of the Proximal Femur Depicted with High-Spatial-Resolution MR Imaging and Multisection CT. *Acad. Radiol.* **2002**, *9*, 1395–1406. [CrossRef]
94. van Oostwaard, M. Osteoporosis and the Nature of Fragility Fracture: An Overview. In *Fragility Fracture Nursing*; Hertz, K., Santy-Tomlinson, J., Eds.; Perspectives in Nursing Management and Care for Older Adults; Springer International Publishing: Cham, Switzerland, 2018; pp. 1–13. ISBN 978-3-319-76680-5. Available online: http://link.springer.com/10.1007/978-3-319-76681-2_1 (accessed on 8 January 2022).
95. Bovik, A.C.; Huang, T.S.; Munson, D.C. The Effect of Median Filtering on Edge Estimation and Detection. *IEEE Trans. Pattern Anal. Mach. Intell.* **1987**, *PAMI-9*, 181–194. [CrossRef] [PubMed]